ABSTRACT

Title of dissertation: LOW LOSS POLYMER NANOPARTICLE COMPOSITES FOR RADIO FREQUENCY APPLICATIONS

Ta-I Yang, Doctor of Philosophy, 2008

Dissertation directed by: Professor Peter Kofinas
Fischell Department of Bioengineering

The aim of this research is to develop novel polymer nanocomposites with desired magneto-dielectric properties including high relative dielectric permittivity (ε_r), high magnetic permeability (μ_r), high ratio of relative permeability to permittivity (μ_r/ε_r), and low energy loss at radio frequencies. In this study, block copolymer-templated and surface-modified magneto-dielectric nanoparticles were utilized because of their ability of uniform dispersion and ordering within the polymer matrices. The influence of intrinsic chemical composition and characteristic lengths (shape and size) of the doped nanoparticles on the resultant composites' magneto-dielectric properties was investigated.

Well-dispersed high-dielectric-permittivity titanium dioxide (TiO_2) nanoparticles were synthesized utilizing a block copolymer as a template. The nanoparticles were confined within microphase separated domains of sulfonated styrene-b-(ethylene-ran-butylene)-b-styrene (S-SEBS) block copolymers. A crosslinker (vinyltrimethoxysilane) was incorporated into the block copolymer matrices in order to decrease the

dielectric loss from the free sulfonic acid groups. Dynamic mechanical analysis experiments confirmed that nanoparticles and crosslinker were confined within the crosslinked sulfonated styrene blocks and had no effect on the chain relaxation behavior of [ethylene-ran-butylene] blocks. Dielectric experiments showed that higher dielectric permittivity composites can thus be obtained with a significant decrease in loss $\tan\delta$ (<0.01) when crosslinked with vinyltrimethoxysilane.

Surfactant-modified iron oxide (Fe_3O_4) and nickel zinc ferrite ($Ni_xZn_{1-x}Fe_2O_4$) nanoparticles of various sizes were successfully synthesized by a seed-mediated growth method. The nucleation and growth of surface-modified nanoparticles was controlled by changing the concentration ratio of surfactant to iron-precursor. The free iron ions present during synthesis are the major factor contributing to the growth of larger particles. The Fe_3O_4 nanoparticle critical size for superparamagnetic to ferrimagnetic transition was determined to be near 30 nm. The dielectric permittivity (ε_r) and magnetic permeability (μ_r) of the resultant block copolymer (styrene-b-ethylene/butylene-b-styrene, SEBS) nanocomposites increased with increasing amount of doped nanoparticles. However, nickel zinc ferrite polymer composites exhibited lower dielectric loss compared to iron oxide composites due to the high electrical conductivity of iron oxide particles. Furthermore, the magnetic permeability (μ_r) of the composites was significantly influenced by the size of the doped nanoparticles. Magneto-dielectric nanoparticles with multi-domain walls lacked the ability to respond to applied alternating field (GHz), thus leading to lower magnetization and magnetic permeability. Superparamagnetic nanopartilces also exhibited lower magnetic permeability due to demagnetization effects from the thermal energy

provided by the nanoparticle surroundings.

LOW LOSS POLYMER NANOPARTICLE COMPOSITES FOR RADIO FREQUENCY APPLICATIONS

by

Ta-I Yang

Dissertation submitted to the Faculty of the Graduate School of the
University of Maryland, College Park in partial fulfillment
of the requirements for the degree of
Doctor of Philosophy
2008

Advisory Committee:
Professor Peter Kofinas, Chair/Advisor
Professor Robert M. Briber
Professor Panagiotis Dimitrakopoulos
Professor Sheryl Ehrman
Professor Srinivasa R. Raghavan

© Copyright by

Ta-I Yang
2008

DEDICATION

To my lovely family, for their endless support.

ACKNOWLEGEGMENTS

Foremost, I would like to thank my advisor, Dr. Peter Kofinas, for his endless support on my Ph.D. studies. Thanks for guiding me to accomplish this research. Thanks for borrowing me your Audi to get the DEA fixed. Thanks for being so patient to proofread my manuscripts. I cannot express enough appreciation for your help, and I would simply like to say I am so honored to be your student.

I would also like to thank my dissertation committee, Dr. Briber, Dr. Raghavan, Dr. Ehrman, and Dr. Dimitrakopoulos, for sharing with me their expertise and research insight. Special thanks to Dr. Kempel for providing magneto-dielectric measurements at GHz frequency range.

Many thanks to the assistance from the former and current members of Kofians' group, Pinar, Linden, Von, Dan, Ayan, Angela, Brendan, Josh, and Rene. They never let me down and were a real support throughout my time at University of Maryland.

I also owe thanks to my friends, Chi-Wei, Shih-Huang, Li-Chung, Xin, Tsao's family, Wu's family, and Ye's family, for their help in numerous ways. I would never forget you, my friends.

Finally, I would like to thank my family. They have always supported and encouraged me to do my best in all matters of life. Especially, thanks to my loving wife, who has been a great source of strength for me to overcome all my struggles. As a Ph.D. in Chemical Engineering, she also inspired me in many aspects of my research. This dissertation would not have been possible without them. I dedicate

this dissertation to them.

Table of Contents

List of Tables

List of Figures

Chapter 1

Introduction

1.1 Motivation

There has been a recent research focus on the development of a class of composite engineered materials made from two or more constituent materials, exhibiting advanced magneto-dielectric properties. These recent reports have shown the potential of artificial materials, often referred to as *metamaterials*, which can significantly extend the range of material properties, enabling the potential for new electromagnetic behavior. The superior properties of metamaterials originate from not only the characteristic length scales and the volume fraction but, more significantly, from the periodic arrangement of constituent magneto-dielectric components within the composite material [1, 2, 3, 4]. There is a need for materials having a wide range of magneto-dielectric properties for applications in microwave communication devices and their miniaturization [5, 6]. Such magneto-dielectric materials must exhibit not only a high relative permittivity (ε_r) and magnetic permeabiltiy (μ_r) but also the desired ratio of the relative magnetic permeability (μ_r) to relative permittivity

(ε_r) [2, 7, 8, 9, 10]. Most importantly, the dielectric loss (tan δ) should be less than 10^{-3}. Therefore, the challenge for making metamaterials is relying on progress in the ability to manipulate the fraction, characteristic length, and arrangement of magneto-dielectric components in the engineered composite. In addition, the weight, shape-flexibility, cost effectiveness and good processability of the material are also key factors for their applications, which are the main reasons why many studies utilize polymeric composites. No systematic study to date has been published on the influence of effective volume fraction, characteristic length, and arrangement of magneto-dielectric components on the effective permittivity (ε) and permeability (μ) of the composites due to the intrinsic incompatibility between inorganic particles and organic matrices. Most published studies utilize the conventional method of blending magneto-dielectric particles into polymers, which has no real control on particle size and dispersion within the polymer matrices [8, 9, 11, 12, 13, 14, 15, 16, 17].

It has been shown in literature that the characteristic length (surface-to-volume ratio) of particles and their distribution and effective volume within the composites will significantly affect the composite's dielectric [18, 19, 20] and magnetic properties [21, 22, 23, 24].

The most promising way to elucidate the effect of all these factors on dielectric and magnetic properties of the composites is to make a nanocomposite, particularly with copolymers which are well-known for their ability to template nanoparticles with narrow size distribution and uniform confinement throughout their periodic microdomains (lamellae, cylinders, or spheres) [3, 25, 26]. The use of block copolymers has been shown to afford opportunities for controlling the spatial distribution

and orientation of the nanocomponents. This allows much more sophisticated tailoring of the overall properties of the composite materials.

An alternative method to manipulate nanoparticles in polymer matrices is to utilize surface-modified nanoparticles. The surface of the nanoparticles is surrounded by a bulky amphiphilic surfactant to prevent agglomeration and provide solubility in different solvents [27]. Such surfactants posses polar groups which will associate with the nanoparticle surface. There is also a bulky component on the surfactant molecule that keeps the nanoparticles away from each other and provides the desired solubility in solvents. Depending on the chemical structure of the bulky component, the surface-modified nanoparticles can dissolve in polar (water) or non-polar solvents (toluene and chloroform) [28, 29, 30, 31]. Therefore, the distribution of magneto-dielectric nanoparticles can be manipulated by utilizing a common solvent for both surfactant-modified particles and polymeric matrices.

The aim of this research is to investigate the influence of intrinsic chemical composition and characteristic lengths (shape and size) of doped nanoparticles on the resultant polymer composites' magneto-dielectric properties. Experiments have been conducted to investigate the feasibility of producing block copolymer-templated and surface-modified magneto-dielectric nanoparticles, leading to uniform dispersion and ordering within polymer matrices. The overall dielectric, magnetic, and mechanical properties of the composites were studied. For some experiments, a crosslinker was incorporated into block copolymer matrices to decrease the dielectric loss. The nanocomposites' permittivity and dielectric loss in the low frequency range (1 to 10000 Hz) was evaluated using a dielectric analyzer (DEA 2970, TA Instruments).

The dielectric and magnetic properties (dielectric permittivity, magnetic permeability and loss tangent) in the Mega- to Giga- frequency range were evaluated using an Agilent RF impedance/material analyzer (E4991A). The results from this research will help develop novel and more manufacturing-friendly methods of manipulating the desirable dielectric and magnetic properties of polymeric composites.

1.2 Dielectric Properties

1.2.1 Dielectric Behavior

Permittivity, $\varepsilon, (Fm^{-1})$ is the ability of a material to be polarized in response to an applied electric field and is defined as

$$\varepsilon \equiv \frac{D}{E} \tag{1.1}$$

where D is the electrical displacement or electrical flux density (Cm^{-2}) and E is electric field strength (Vm^{-1}).

A high permittivity tends to reduce any electric field present. The permittivity of free space or vacuum, ε_0, has a value of $8.9 \times 10^{-12}\ Fm^{-1}$. The permittivity of a material is usually given relative to that of free space, and is known as relative permittivity, ε_r, or dielectric constant, k. The permittivity is then calculated by multiplying ε_0 with ε_r. Capacitance, C, $(F, farad)$, which is a direct measure of the ability of the material to store electrical energy when the charging of capacitor plates to the applied potential difference is completed is defined as:

$$C \equiv Q/V = \varepsilon \cdot A/d \tag{1.2}$$

where Q is the accumulated charge, V is the voltage difference between the electrodes, A is the electrode surface area, and d is the thickness of material between electrodes.

This formula states that the applied voltage will induce a charge Q because structural elements of any material are susceptible to polarization and effectively electrical dipoles are created within that material.

The dielectric constant of any given material is directly proportional to its polarizability and the basic mechanisms of polarization in dielectrics include: electronic polarization (α_e), atomic or ionic polarization (α_i), orientation polarization (α_o), and interface polarization (α_{inter}) [32, 33, 34].

- Electronic polarization (α_e): an electrical field will always displace the center of charge of the electrons with respect to the nucleus and thus induce a dipole moment due to separation of positive and negative charge center in an atom.

- Atomic or ionic polarization (α_i): observed due to the change of distance between positive and negative ions. The external field induces net dipoles by slightly displacing the ions from their rest position, leading to ionic polarization.

- Orientation polarization (α_o): observed due to reorientation of the existing dipoles. The material must have natural dipoles which can freely rotate. The

external field aligns these dipoles to some extent and thus induces a polarization of the material.

- Interface polarization polarization (α_{inter}): surfaces, grain boundaries, interface boundaries (including the surface of precipitates) may be charged, i.e. they contain dipoles which may become oriented to some degree in an external field and thus contribute to the polarization of the material.

The combined polarization, $\sum_j \alpha_j$, is expressed by:

$$\sum_j \alpha_j = \alpha_e + \alpha_i + \alpha_o + \alpha_{inter} \tag{1.3}$$

1.2.2 Dielectric Loss

The net effects of the polarization of a dielectric material in an applied sinusoidal alternating field causes phase retardation of current by some angle δ, due to the inertia of the electric charge movement in the applied field. As a result, the current, I, advances the voltage ,V, by (90^0- δ). The dielectric response at various frequencies is described in terms of the complex permittivity (ε^*) which is represented by its real and imaginary parts.

$$\varepsilon^* = \varepsilon' - i\varepsilon'' \tag{1.4}$$

where ε' is the permittivity or the dielectric storage (decreases with increasing frequency) and ε'' is the dielectric loss factor (may increase or decrease with increasing frequency). The phase angle δ is related to ε' and ε''as follows:

$$\tan\delta \equiv \frac{\varepsilon''}{\varepsilon'} \tag{1.5}$$

$\tan\delta$ is usually called the dielectric loss tangent ($\tan\delta$) or dissipation factor (D).

The dielectric processes such as dipole relaxation or space charge formation contribute to both the permittivity and loss behavior. The dielectric loss factor is made up of two components; one is due to relaxation or space-charge conduction processes and the other is due to the direct current (DC) conduction of the material [35]. Furthermore, the dielectric loss of a material is also heavily influenced by extrinsic factors such as its microstructure defects or porosity [32].

1.2.3 Effective Dielectric Function of Inhomogeneous Media

In past decades, there have been numerous approximate analytical theories developed to predict and calculate the effective dielectric function of macroscopically inhomogeneous media. In those mixture models the effective dielectric permittivity of a composite material is defined as a complicated function of the permittivity of every constituent particle depending on its size, shape, and volume fraction. Several comprehensive reviews of dielectric mixture models have been published in literature [18, 19, 20].

The Maxwell-Garnett (MG) [36] and Bruggeman self-consistent effective medium approximations [37] are the classic methods for the effective dielectric function of inhomogeneous media and have been modified to various derivatives [19, 20].

- Maxwell-Garnett (MG) Approximation

The MG approach assumes that one of the phases, a dilute suspension of spherical particles (an inclusion phase) with dielectric function ε_2, is inside a continuum matrix phase with dielectric function ε_1, and both phases are embedded in an effective media (reference homogeneous medium) with dielectric function ε_{eff}. The particle volume fraction Φ_2 is assumed to be much smaller than one and the particle diameter d is believed to be well below the wavelength λ of light [36]. This model includes the interaction between spherical inclusions. It is, however, only valid for low inclusion concentrations.

$$\varepsilon_{eff} = \varepsilon_1 \cdot \left(1 + \frac{3\Phi_2\beta}{1 - \Phi_2\beta}\right) \tag{1.6}$$

where $\beta = \dfrac{\varepsilon_2 - \varepsilon_1}{\varepsilon_2 + 2\varepsilon_1}$

- Bruggeman Equation

  The classical (symmetrical) Bruggeman equation (BE) was pioneered by Bruggeman. In this theory a typical element of the two-phase composite is embedded in an effective medium whose properties are to be determined self-consistently. It should be noted that the Bruggeman equation (BE) does not contain parameters signifying the system microgeometry. As a consequence the BE gives the fixed percolation threshold $f_c = 1/d$, where d is the space dimensionality [37].

$$(1 - q_2)\,\frac{\varepsilon_1 - \varepsilon_{eff}}{\varepsilon_1 + 2\varepsilon_{eff}} + q_2\frac{\varepsilon_2 - \varepsilon_{eff}}{\varepsilon_2 + 2\varepsilon_{eff}} = 0 \tag{1.7}$$

  The above equation is known as the symmetric Bruggeman formula, where

ε_1 is the dielectric constant of component 1 and ε_2 is the dielectric constant of component 2 with volume fraction q_2 . The non-symmetric Bruggeman equation is represented by

$$\frac{\varepsilon_2 - \varepsilon_{eff}}{\varepsilon_2 - \varepsilon_1} = (1 - q_2) \left(\frac{\varepsilon_1}{\varepsilon_{eff}} \right)^{\eta} \tag{1.8}$$

where η is the space dimensionality of component 2 [20]. $\eta = -\frac{1}{3}$ for spherical [19] and $\eta = -\frac{1}{2}$ for disk component [38].

1.3 Magnetic Properties

1.3.1 Magnetic Permeability (μ)

The magnetic permeability (μ) characterizes the net induced magnetic flux density (B) when a material presents inside a helical winding wire and an applied magnetic field (H) acting on it [39].

$$\mu \equiv \frac{B}{H} \tag{1.9}$$

where H is magnetic field (A/m) and B is magnetic induction or magnetic flux density ($Teslas$, Vs/m^2).

The net induced magnetic flux density (B) is the sum of that of the vacuum and that due to the material, and can also be expressed as follows:

$$B = \mu_0(H + M) = \mu_0 H(1 + \chi) = \mu_0 H \mu_r \tag{1.10}$$

where μ_0 is magnetic permeability of vacuum ($4\pi \cdot 10^{-7} Vs/Am$), $\mu_r (= \mu/\mu_0)$ is the relative permeability of the material, M is the material's magnetization (A/m), and χ is the magnetic susceptibility.

Type	Magnetic susceptibility(χ)
Diamagnetic	$\approx -10^{-6}$
Paramagnetic	$\approx +10^{-3}$
Ferromagnetic	Extremely large and positive
Ferrimagnetic	Large and positive
Antiferromagnetic	Small and positive

Table 1.1: Classification of magnetic materials based on their magnetic susceptibility(χ) values [19].

In terms of relative permeability, the magnetic susceptibility is expressed by:

$$\chi = \mu_r - 1$$

The magnetic behavior of various kinds of materials can be characterized by their χ values, as shown in Table 1.1 [19].

In an alternating magnetic field, the magnetic response at various frequencies is described in terms of the complex permeability (μ^*) which is represented by its real and imaginary parts.

$$\mu^* = \mu' - i\mu'' \tag{1.11}$$

where μ' is the inductive component or real part of the permeability and μ'' is the resistive component or imaginary part of the permeability.

The phase angle δ is related to μ' and μ''as follows:

$$\tan\delta \equiv \frac{\mu''}{\mu'} \tag{1.12}$$

$\tan\delta$ is usually called the magnetic loss tangent.

1.3.2 Magnetic Domains and Hysteresis

Bulk ferromagnetic or ferrimagnetic materials at a temperature below their Curie temperatures consist of a large number of small magnetic domains, and each one is spontaneously magnetized to its saturation magnetization. Adjacent domains are separated by domain boundaries or walls as shown in Figure 1.1 [40]. The char-

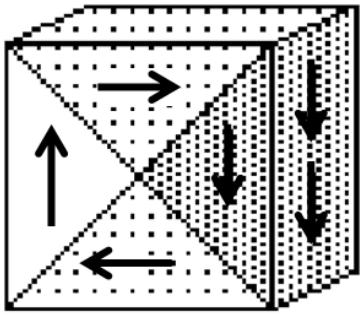

Figure 1.1: Schematic magnetic domains in ferromagnetic materials [40].

acteristic hysteresis behavior between M and H of ferromagnetic (or ferrimagnetic) materials results from the presence of magnetic domains. At the demagnetized state, there is no net M field due to the magnetic moments of the constituent domains randomly oriented. As the external field applied, the domains are oriented in directions favorable to the applied field by stretching, moving, combining their domain walls (Figure 1.2a). This process continues with increasing field strength until mag-

netic materials become a single domain, and the corresponding magnetization is the saturation magnetization M_s, as shown in Figure 1.2b. However, as the H field is reduced by reversal of field direction, the domain walls are unable to fully reverse their motion back to their original positions. As a result, the magnetization curve shows hysteresis, and some magnetization (remanent magnetization, M_r) remains in the materials even when the field is completely removed. The coercive field or coercivity (H_c) is defined to be the additional field, applied in the reverse direction, which is needed to reduce the magnetization to zero [41]. Magnetic materials are usually characterized as "hard" or "soft", depending on the magnitude of their coercivity (H_c) as shown in Figure 1.3 [43]. Typically, a "hard" magnetic material's coercivity is above 150 kAm^{-1} and a "soft" magnetic material's coercivity is below 50 Am^{-1}.

1.3.3 Superparamagnetism

The properties of magnetic nanoparticles are dramatically different from their bulk counterparts. Specifically, their magnetization significantly depends on particle characteristic length.

The anisotropy energy sustaining the particle's magnetization is given by the product of the anisotropy constant, K, and the volume of the particles, V. The most common types of anisotropy are:

- Magnetocrystalline anisotropy: magnetocrystalline anisotropy arises from spin-orbit coupling and energetically favors alignment of the magnetization along

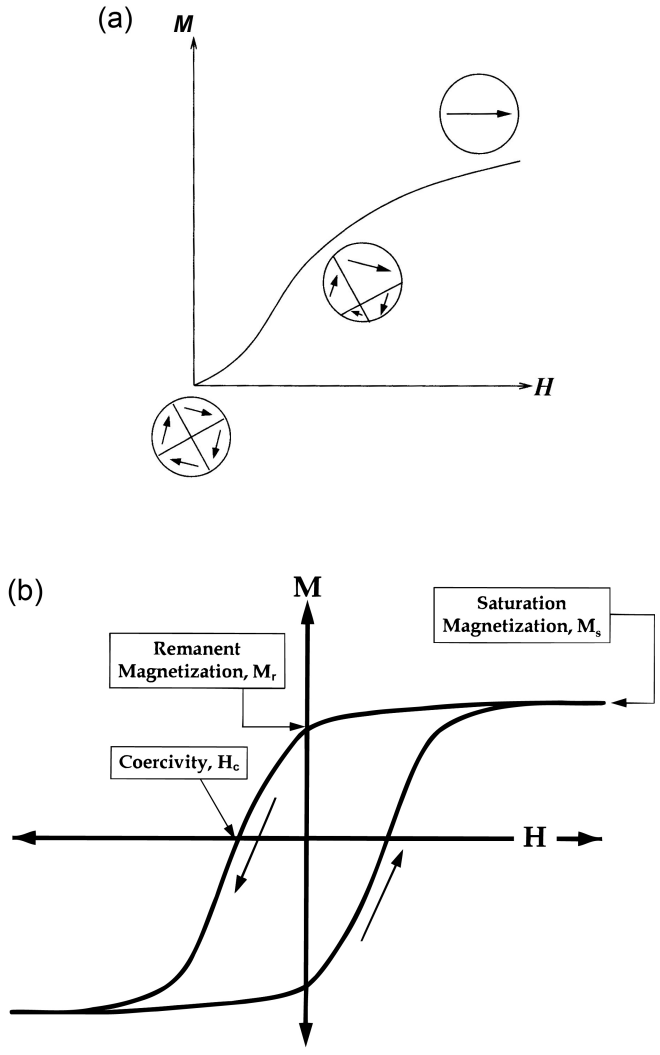

Figure 1.2: (a) Change in domain structures of ferromagnetic materials during magnetization. (b) Magnetic $M - H$ hysteresis loop of ferromagnetic materials [42].

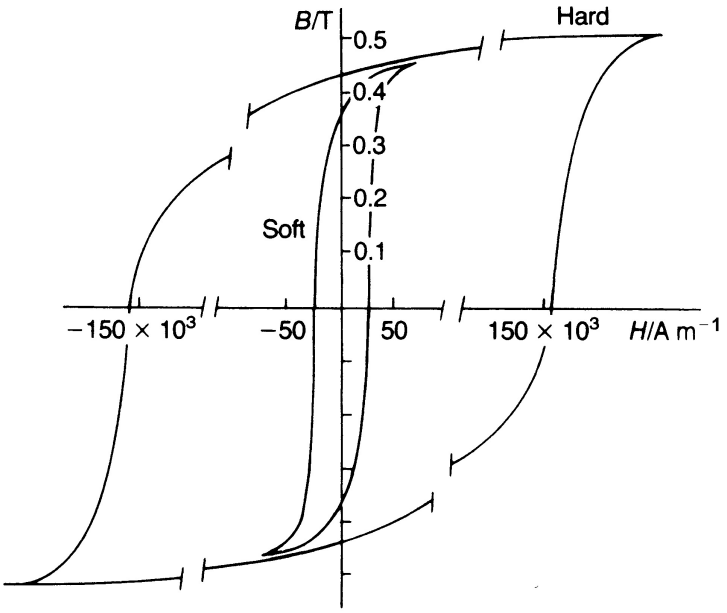

Figure 1.3: Typical $B - H$ hysteresis loops for "soft" and "hard" materials [43].

a specific crystallographic direction. A polycrystalline magnetic material with no preferred grain orientation has no net magnetocrystalline anisotropy due to cancelation over all orientations [42].

- Shape anisotropy: the origin of this anisotropy can be visualized by considering the difference in magnetostatic energy in a non-spherical particle [44]. The demagnetizing field is stronger for a short axis than for a long one. A magnetic material with spherical shape have no overall shape anisotropy. If the material is not spherical, then it will be easier to magnetize it along a long axis. For a prolate of cobalt, as an example, Figure 1.4 shows the shape anisotropy constant as a function of the c/a ratio [41].

- Exchange anisotropy: it occurs when a ferromagnet is in close proximity to

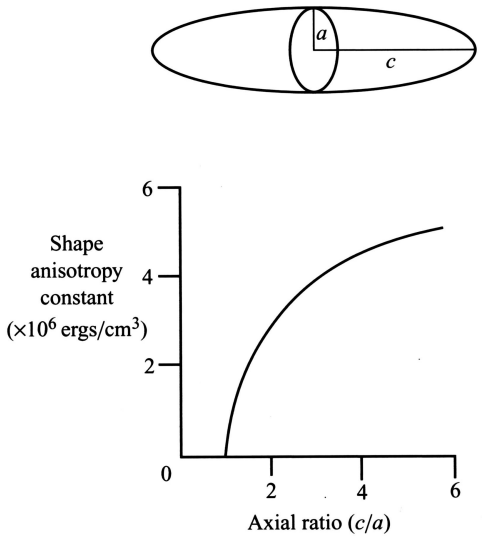

Figure 1.4: Shape anisotropy constant in a prolate spheroid of cobalt [41].

an antiferromagnet or ferrimagnet. Magnetic coupling at the interface of the two materials can create a preferential direction in the ferromagnetic phase, which takes the form of a unidirectional anisotropy [42].

- Surface anisotropy: surface anisotropy results from the lack of translational symmetry at the boundaries of particles due to the existence of broken magnetic exchange bonds, leading to surface spin disorder and frustration [23, 42, 45]. It becomes important and more prominent when the particle size is near 2 nm [23, 46].

As the size of the magnetic particles is reduced from the bulk, there are only single magnetic domains present without any domain walls existing in particles below a certain critical size (D_{SD}) [21, 22, 23]. However, as the the particle size decreases below D_{SD}, the KV product becomes comparable to the thermal energy provided by the surroundings, k_bT, where k_b is Boltzmann's constant and T is

temperature, respectively. As a result, the anisotropy energy cannot sustain the magnetization of the particles due to thermal energy effects, and the system becomes superparamagnetic [24, 42]. Superparamagnetism can be overcome by reducing the system's temperature, increasing particle size, or increasing the shape anisotropy (e.g. irregular particle shape results in larger shape anisotropy), so that KV becomes larger than k_bT [41].

1.3.4 Effective Magnetic Function of Inhomogeneous Media

The theoretical description of effective properties of magnetic composites is a difficult task. This is due to a specific form of non-linear dependence of the local magnetic permeability of the ferromagnetic phase on the magnetic field [47]. Most published work on this subject is derived from the conventional Maxwell-Garnett (MG) approximation and Bruggeman effective medium approximation, but there are no general solutions satisfactory for different cases [48, 49, 50]. However, it could be concluded that the volume fraction and shape of the embedded-particle and its distribution within the composite significantly affects the bulk composite magnetic properties.

1.4 Block Copolymers

Block copolymers are known for their ability to spontaneously form self-assembled periodic patterns with length scales on the order of 10's to 100's of nanometers in bulk and in solutions, resulting in a range of different periodic morphologies (e.g.,

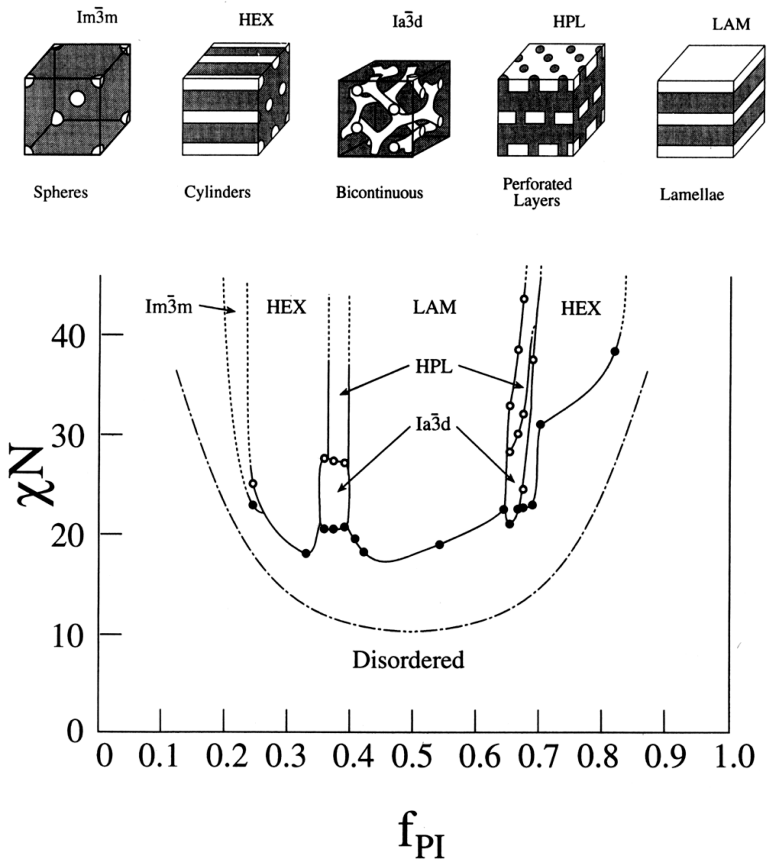

Figure 1.5: Experimentally-determined phase diagram for PS-PI diblock copolymers [54].

lamellae, cylinders, or spheres are typically observed)[51]. For AB-diblock copolymers the basic parameters that determine the size and shape of the microdomains are: the degree of polymerization N ($N = N_A + N_B$), the composition $f_A = N_A/N$, and the Flory-Huggins interaction parameter χ_{AB} representing chemical nature of the blocks [52, 53]. Figure 1.5 shows the experimentally-determined poly(isoprene-b-styrene) diblock copolymers microphase separation diagram [54].

For ABA-triblock copolymers examined using self-consistent field theory (SCFT), their phase behaviors are similar with diblock copolymers with slightly larger domain

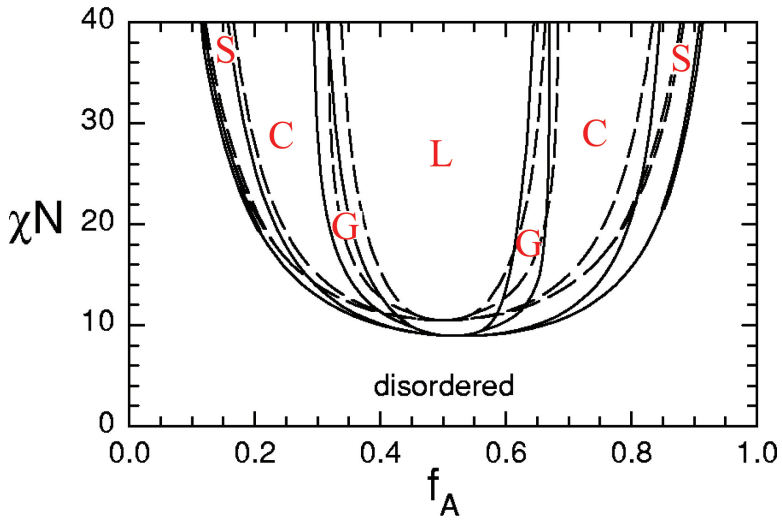

Figure 1.6: Phase diagram of diblock (dashed curves) and triblock (solid curves) copolymers [55]. The ordered phases are labeled as L (lamellar), G (gyroid), C (cylindrical), and S (spherical).

spacings, as shown in Figure 1.6 [51, 55]. Methods including solvent and temperature annealing, electric fields, and mechanical flow fields, are applied in order to achieve fully-developed microphase separation [26, 56].

Further, the periodic block patterns of block copolymers can be selectively decorated both chemically and physically, making block copolymers ideal systems to manipulate the overall properties of the composite materials. Many researchers have demonstrated that nanoparticles of metals, semiconductors, or magnetic oxides can be incorporated selectively or synthesized in situ in nanodomains of block copolymers [3, 25, 26]. The locations of these incorporated nanoparticles within block copolymers were determined by the nanoparticles' surface properties [57, 58, 59, 60].

1.5 Surface-modified Nanoparticles

There has been a challenge for researchers to stabilize magnetic nanoparticles which tend to agglomerate due to van der Waals and magnetic attractions. The most common method to prevent nanoparticles from agglomeration is to passivate the high energy surfaces of the nanoparticles by attaching a bulky amphiphilic surfactant or ionic polymer [27]. The amphiphilic surfactant or ionic polymer generally possess a hydrophilic and a hydrophobic part. The polar groups in the hydrophilic part can associate with the nanoparticle surface. The bulky hydrophobic component provides the steric isolation to prevent van der Waals attraction and magnetic attraction from magnetic particles, causing the agglomeration of nanoparticles. Furthermore, surface-modified nanoparticles can dissolve in polar solvents (water) [61, 62, 63] or non-polar solvents (toluene and chloroform) [28, 29, 30, 31], depending on the chemical affinity of the bulky component to the solvents. Many studies have showed Fe [30], $CoFe_2O_4$ [31, 64], Fe_3O_4[29, 31, 64] and γ-Fe_2O_3 [65] magnetic nanoparticles with narrow size distribution and no agglomeration can be synthesized by utilizing oleic acid as the surface modifying surfactant.

1.6 High Dielectric Permittivity Polymeric Composites

High dielectric permittivity (ε) polymer-based shape conforming composites have potential for applications in microwave communication devices [5], artificial muscles [66], and embedded capacitors for microelectromechanical systems [67, 68]. Weight, shape-flexibility, cost effectiveness and good processability of the material

are also the key factors for these applications, which is the main reason why many research efforts utilize polymeric composites.

The most common process for enhancing the dielectric permittivity of a polymer is to disperse a high-dielectric-permittivity ceramic powder such as barium titanate ($BaTiO_3$) [67, 69, 70] and lead titanate ($PbTiO_3$) [71] into polymers to form composites. In order to obtain a high value of dielectric permittivity, large amount of fillers have to be loaded, resulting in loss of flexibility and inhomogeneous composites. Another approach to obtaining high dielectric permittivity composites is to utilize conductive fillers (near their percolation threshold) to produce the composites. By dispersing conductive particles, e.g., carbon nanofibers [69, 70], silver particles [68] and copper phthalocyanine oligomers [66, 72] into a polymer matrix, it has been demonstrated that the dielectric permittivity of the polymer significantly increases. The increased dielectric permittivity observed in such composites arises from conducting particles isolated by very thin dielectric layers to form micro-capacitors. However, the dielectric loss is very high and difficult to control, because the particles can easily form a conductive path in the composite as the filler concentration nears the percolation threshold.

1.7 Polymeric Magneto-dielectric Composites

Materials having a wide range of magneto-dielectric properties are promising for advanced applications in microwave communication devices including static dissipative and electromagnetic interference (EMI)/radio frequency interference (RFI)

shielding devices [73, 74, 75, 76, 77], antennas [75, 78], and radomes [75]. Such magnetodielectric materials must exhibit not only a high relative dielectric permittivity (ε_r) which allows the size of a microwave device to be scaled by $(\mu_r\varepsilon_r)^{-1/2}$ [6], but also the desired ratio of relative permittivity (ε_r) to relative magnetic permeability (μ_r) [2, 8, 9, 10].

For antenna applications, the miniaturization factor and wave impedance are respectively proportional to the square-root of the product and ratio of the relative permeability (μ_r) and relative dielectric permittivity (ε_r). This means that for a higher value of μ_r or ε_r, a smaller antenna can be obtained and with a higher ratio of μ_r to ε_r, a wider bandwidth will be available [2, 10]. For example, the bandwidth for antenna applications could be improved by a factor of 13, when the μ_r/ε_r ratio is equal to 3, while keeping $\mu_r \cdot \varepsilon_r = 25$ [10]. The bandwidth (BW) for an antenna with thickness t can be approximated by

$$BW \approx \frac{96\sqrt{\frac{\mu_r}{\varepsilon_r}}\frac{t}{\lambda_0}}{\sqrt{2}\left[4 + 17\sqrt{\mu_r\varepsilon_r}\right]} \tag{1.13}$$

For application in electromagnetic wave absorption [7, 8], the goal is to manipulate the μ_r and ε_r in order to obtain zero reflection ($Z_{in} = 1$).

$$Z_{in} = \sqrt{\frac{\mu_r}{\varepsilon_r}} \tanh\left[j\frac{2\pi t}{\lambda_0}\sqrt{\mu_r\varepsilon_r}\right] \tag{1.14}$$

where λ_0 is the wavelength of microwave in free space and t is the thickness of an absorber.

$$\text{reflection loss (dB)} \ = 20\log\left(\frac{Z_{in} - 1}{Z_{in} + 1}\right) \tag{1.15}$$

Ferrites are mixed crystals of various metallic oxides and have the general formula: $MOFe_2O_3 \cdot xH_2O$ where M is a divalent metallic ion such as Fe^{2+}, Sr^{2+}, Ba^{2+},Mn^{2+},Ni^{2+},Zn^{2+},Mg^{2+}, and Co^{2+} [19, 79]. The superior properties of ferrites such as high resistivity, high permeability, and low dielectric loss have made them attractive for applications in microwave devices [80, 81]. Various ferrite/polymer composites have been developed for microwave antenna and electromagnetic wave absorption applications. The most common method to fabricate these composites was to blend magnetic particles into polymers [12, 15, 16] and others also embedded ferrite particles into conducting polymer matrices using an oxidative electrochemical polymerization process [82] or a UV irradiation method [83]. Such methods lack control on particle size and distribution within the polymer matrix. Surface-modified magnetic nanoparticles have been developed to improve the compatibility with polymer matrices. The size and shape of the surface-modified nanoparticles are controllable by introducing amphiphilic surfactants or ionic polymers during synthesis [27]. Many studies have shown that Fe [30], $CoFe_2O_4$ [64], Fe_3O_4 [29, 64] and γ-Fe_2O_3 [65] magnetic nanoparticles with narrow size distribution and no agglomeration can be synthesized with modifying surfactants. However, such nanoparticles are superparamagnetic, which means that the particles are easily demagnetized by thermal fluctuations from the environment they are in.

Chapter 2

Block Copolymer Templated High Dielectric Permittivity Nanoparticles

2.1 Introduction

In this study, high dielectric permittivity polymer-based composites were prepared utilizing a block copolymer. The nature of the self-assembled nanoscale morphology of the block copolymer enables the formation of stable particles uniformly dispersed within the polymer matrix. Furthermore, the dielectric loss of a material, which limits frequency selectivity, is heavily influenced by factors such as ionic conduction and structural heterogeneities (microstructure defects or porosity), which will generate flow of charges and results in thermal dissipation of energy [35]. Block copolymer nanocomposites could significantly reduce such factors causing dielectric loss by providing insulation layers and highly periodic templated nanoparticles.

Sulfonated [styrene-b-(ethylene-ran-butylene)-b-styrene] (S-SEBS) block copolymers containing sulfonic acid groups (SO_3H) were selected to investigate their ability to template nanoparticles within their self-assembled microstructures. In or-

der to obtain high dielectric permittivity particles, organic complexes of titanium were selected to form titanium dioxide (TiO_2) nanoparticles which preferentially associate with sulfonic acid groups of one of the blocks of the copolymer. Upon solvent evaporation and film casting, nanoparticles are formed via a hydrolysis reaction uniformly distributed within the polymer matrix, which acts as a template to enhance the ordering of the high dielectric permittivity nanoparticles. The crosslinker (vinyltrimethoxysilane) was also incorporated into S-SEBS block copolymers to study its effect on dielectric and mechanic properties of the composites. The composites were characterized by X-ray photoelectron spectroscopy (XPS), dynamic mechanical analysis (DMA), and dielectric analysis (DEA).

2.2 Experimental Section

Materials: Titanium acetylacetonate (TYZOR AA105) was supplied by E.I. du Pont de Nemours and Company. Sulfonated [styrene-b-(ethylene-ran-butylene)-b-styrene] (S-SEBS) block copolymer solution and vinyltrimethoxysilane were purchased from Aldrich. The molecular weight of the S-SEBS block copolymer was 80,000 g/mol consisting of 29 wt% styrene blocks and 59.7 mol% of styrene blocks sulfonated. All chemicals were used as received without further purification.

S-SEBS templated titanium dioxide (TiO_2) nanoparticles: Titanium acetylacetonate was selected as the precursor to form the TiO_2 nanoparticles. The S-SEBS solutions were mixed with different concentrations of precursors, where the molar ratio between SO_3H groups of S-SEBS and Ti was 100: 2, 4, 16, 32, 48 ,and

128. The solution was vigorously stirred for 30 minutes. The Ti organometallic complexes preferentially attached to the sulfonated styrene blocks. A solid film was formed by static casting over a period of one week. The Ti organometallic complexes attached to the SO_3H groups were gradually hydrolyzed and formed titanium oxide nanoparticles within the sulfonated styrene blocks.

S-SEBS templated titanium dioxide (TiO_2) composites with crosslinker: The procedure was the same as for synthesis of S-SEBS templated TiO_2, except that both vinyltrimethoxysilane crosslinker and TiO_2 precursors were simultaneously added to S-SEBS polymer solutions. The molar ratio of crosslinker to SO_3H groups within the copolymer was kept at 2.5 while the molar percentage of Ti/SO_3H varied from 2 to 64. The solution was vigorously stirred for 30 minutes, then poured into a teflon boat. A solid film was formed by static casting over a period of one week. The resulting films were placed in an oven for heat-treatment at 150 °C for 24 hours and exposed to UV light (260-320 nm) for 20 minutes at 150 °C.

Characterization: X-ray photoelectron spectroscopy (XPS, AXIS 165, Kratos) was used to investigate the oxidation state of titanium. The charge-shifted spectra were corrected assuming that the adventitious $C1s$ peak detected was at 284.600 eV. Dielectric measurements for the resulting S-SEBS nanocomposites were performed using a dielectric analyzer (DEA 2970, TA Instruments). The samples were sandwiched between the ceramic parallel plate sensors, and subjected to a force of 200 N. The DEA cell was purged with dry nitrogen at a flow rate of 500 mL/min for 30 minutes to ensure the absence of moisture during measurements. The experiments were performed at frequencies of 1, 5, 10, 22, 46, 100, 215, 464, 1000, 2150, 4640, 10000

Hz at 35 $^{\circ}C$. Transmission electron microscopy (TEM, HITACHI H-600) operated at 100 keV was used to observe the morphology of the composites. The samples for TEM were prepared by solvent casting directly onto a copper grid and were visualized without any staining to enhance TEM contrast. Tensile strength and ultimate elongation, as well as storage and loss modulus transitions were studied with a dynamic mechanical analyzer (DMA Q800, TA Instruments). Thermogravimetric analysis (TGA-50, SHIMADZU) was utilized to investigate the thermal stability of the composite. Samples were heated at 10 $^{\circ}C$/min under ambient conditions.

2.3 Results and Discussion

2.3.1 Templated Titanium Dioxide (TiO_2) Composite Morphology

The morphologies of the nanocomposites were investigated by transmission electron microscopy (TEM). The pure S-SEBS block copolymer without any templated particles exhibited a microphase separated morphology, shown in Figure 2.1. The micro-phase separated morphology was observed without any TEM staining. TEM constrast results from atoms of heavier atomic number. It is believed that the sulfonic acid groups (59.7 mol%) on the sulfonated styrene blocks provided the contrast (darker stripes) for the TEM image. For the S-SEBS block copolymer mixed with TiO_2 precursors, the resulting nanoparticles were confined within the darker stripes containing the sulfonated styrene blocks, as shown in Figure 2.2.

This experiment showed that sulfonic acid groups (SO_3H) can preferentially

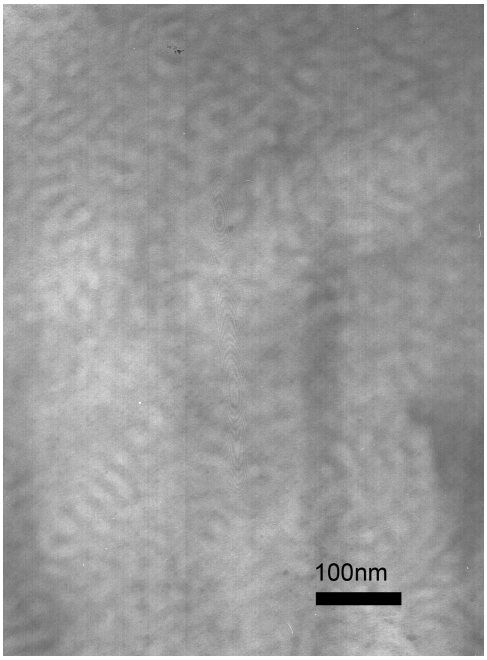

Figure 2.1: TEM image of S-SEBS block copolymer.

associate with titanium organometallic complexes (Tyzor AA105) and then template the TiO_2 nanoparticles within self-assembled microstructures of the S-SEBS block copolymers for Ti/SO_3H molar ratios below 0.48. High-resolution XPS experiment determined the oxidation state of the nanoparticles, as shown in Figure 2.3. The binding energies of Ti $2p_{1/2}$ (464.15eV) and $2p_{3/2}$ (458.50eV) are in agreement with existing literature and are characteristic of titanium dioxide (TiO_2) [84, 85].

However, when Ti/SO_3H molar ratio was larger than 1.28, TiO_2 nanoparticles not only formed within the styrene block domain (Figure 2.4a), but also became bigger and non-uniform particles ($\approx$ 80nm) randomly dispersed inside the polymer matrix (Figure 2.4b).

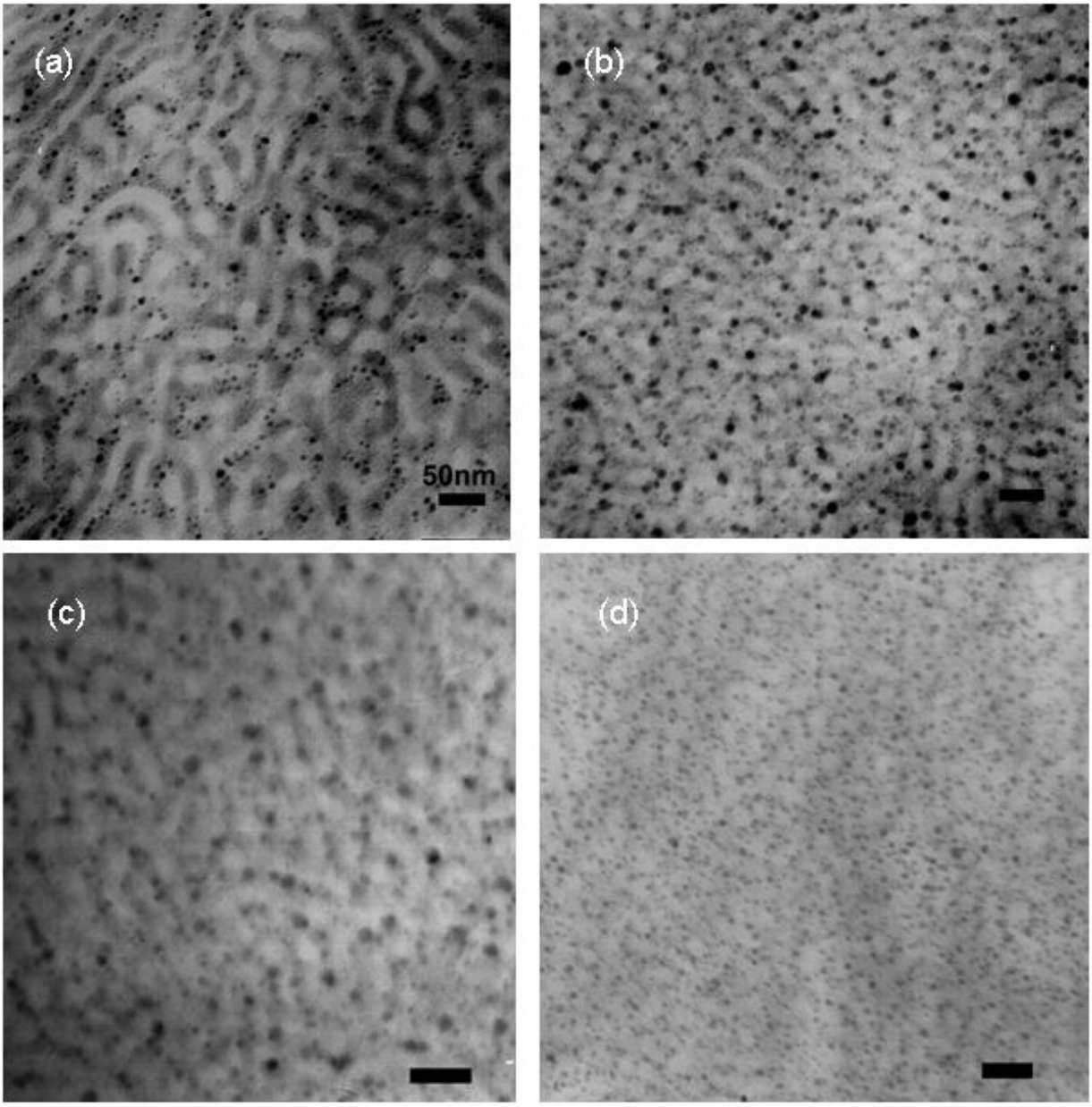

Figure 2.2: TEM images of S-SEBS doped with different Ti/SO_3H molar ratios. (a)0.02, (b)0.04, (c)0.16, (d)0.32. (scale bar = 50 nm)

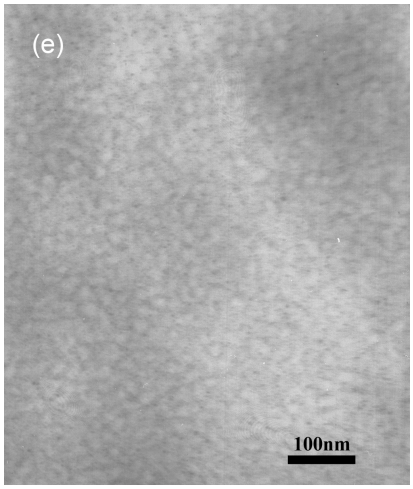

Figure 2.2: TEM images of S-SEBS doped with different Ti/SO_3H molar ratios. (cont'd) (e)0.48.

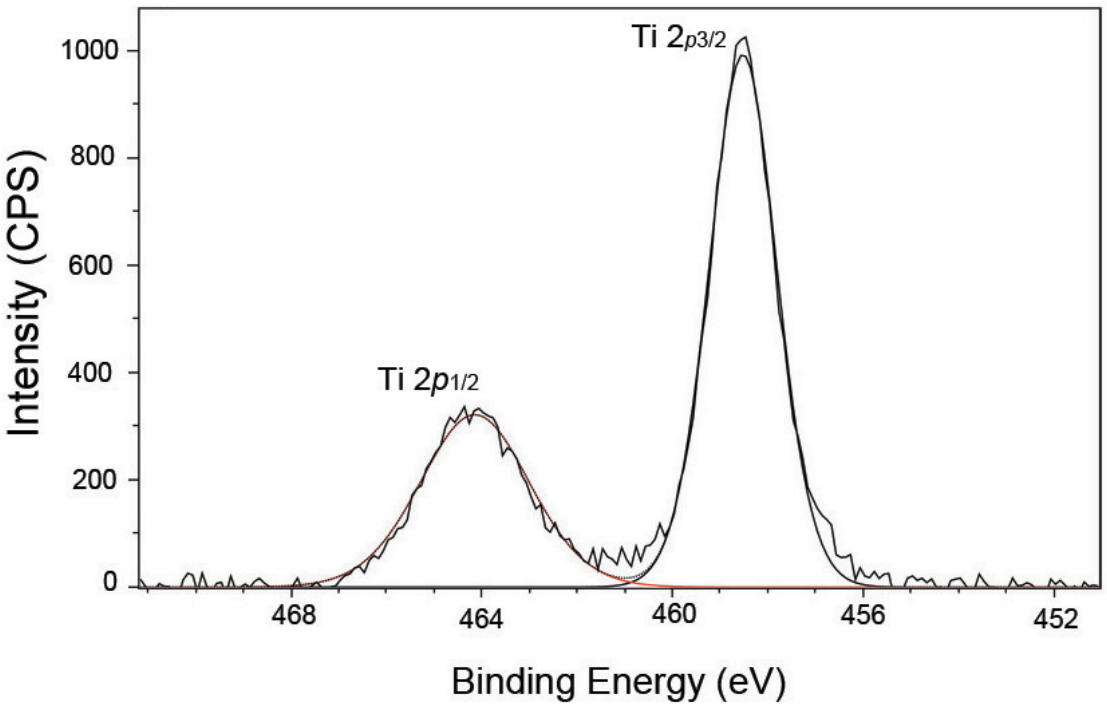

Figure 2.3: XPS spectra of S-SEBS block copolymer composite with templated TiO_2 nanoparticles.

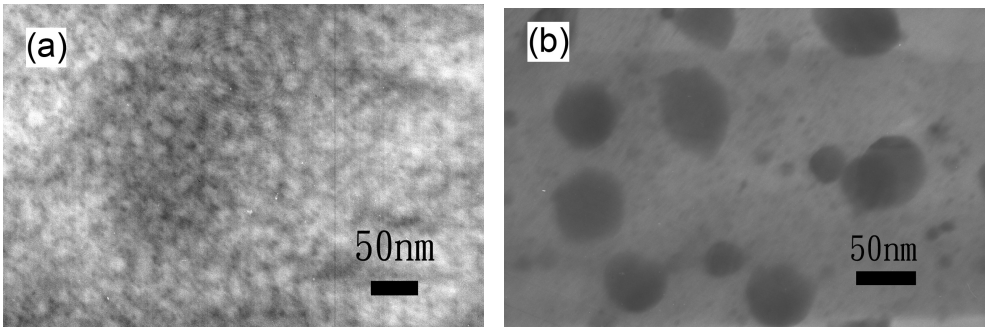

Figure 2.4: TEM images of S-SEBS doped with 1.28 of Ti/SO_3H molar ratio.

2.3.2 Composite Morphology of Templated TiO_2 with Crosslinker

It has been reported that sulfonic acid groups significantly contribute to proton conductivity which leads to increase in the dielectric loss of the composite [86]. In order to reduce the dielectric loss resulting from the mobile protons in the sulfonic acid groups of S-SEBS copolymers, the crosslinking reagent vinyltrimethoxysilane was introduced into the sulfonated styrene block of S-SEBS to remove the protons of the sulfonic acid groups (SO_3H) [87, 88].

The block copolymer microphase separated morphology (Figure 2.5) for the S-SEBS with crosslinker (the molar ratios of crosslinker to the SO_3H groups were 0.5, 2.5, and 5.5) showed the same morphology as the uncrosslinked S-SEBS block copolymer except that the contrast for the TEM imaging was more enhanced. The crosslinker tends to preferentially associate with SO_3H groups through hydrogen bonds and therefore enhance the contrast. In addition, the un-changed glass transition temperature of the [ethylene-r-butylene] block also indicates the crosslinker was excluded from [ethylene-r-butylene] block (see Section 2.3.3). These experiments therefore confirmed that the crosslinker was confined within the sulfonated styrene

blocks. However, both TiO_2 nanoparticles and crosslinks could not be simultaneously formed within the sulfonated styrene block when molar ratios of crosslinker and Ti precursor to the SO_3H groups were 5.5 and 0.04, respectively (Figure 2.6b). Crosslinkers tend to compete with TiO_2 precursors for associating with available SO_3H groups. Therefore, lower amounts of crosslinkers (molar ratio=2.5) ensure formation of crosslinks and TiO_2 nanoparticles well dispersed within the sulfonated styrene domains (Figure 2.6a).

The morphologies of the S-SEBS titanium dioxide (TiO_2) composites with crosslinker showed that the TiO_2 nanoparticles were confined within the sulfonated styrene blocks with the morphology being unaffected (domain=15nm) by simultaneous addition of crosslinker and TiO_2 precursors (see Figure 2.7). The molar ratio of crosslinker to SO_3H groups within the copolymer was kept at 2.5 while the molar ratios of Ti/SO_3H varied from 0.02 to 0.32. However, there is no distinct morphology showing the TiO_2 nanoparticles confined within specific blocks when adding 0.48 of Ti/SO_3H molar ratio(Figure 2.8a). The TiO_2 nanocomposite became brittle and broke apart with 0.48 of Ti/SO_3H molar ratio added, indicating that the polymer was over-doped with TiO_2 nanoparticles (Figure 2.8b).

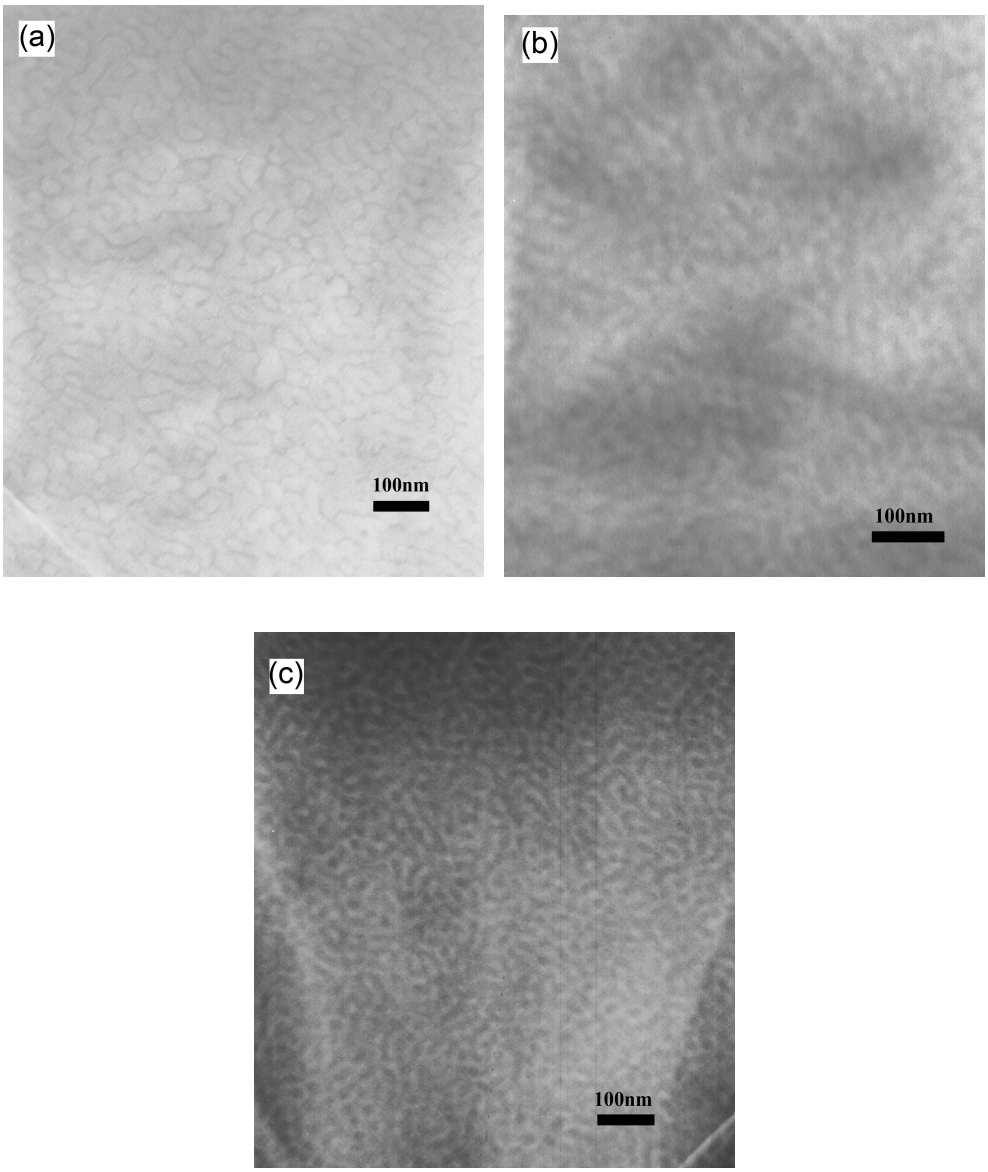

Figure 2.5: TEM images of S-SEBS mixed with different molar ratios of crosslinking agent. (a)0.5, (b)2.5, (c)5.5.

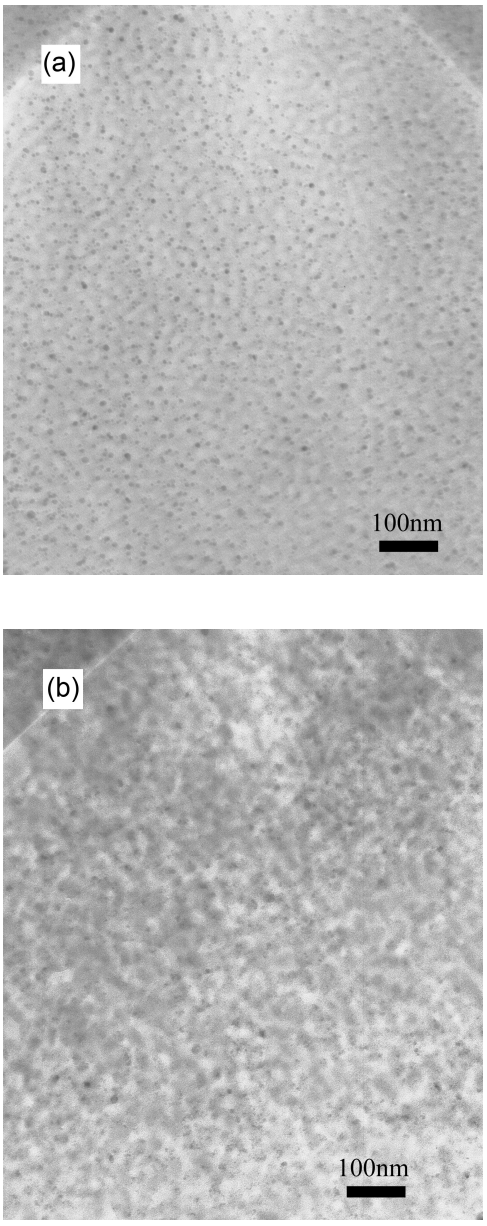

Figure 2.6: TEM images of S-SEBS doped with 0.04 of Ti/SO_3H molar ratio and different molar ratios of crosslinking agent: (a)2.5, and (b)5.5 .

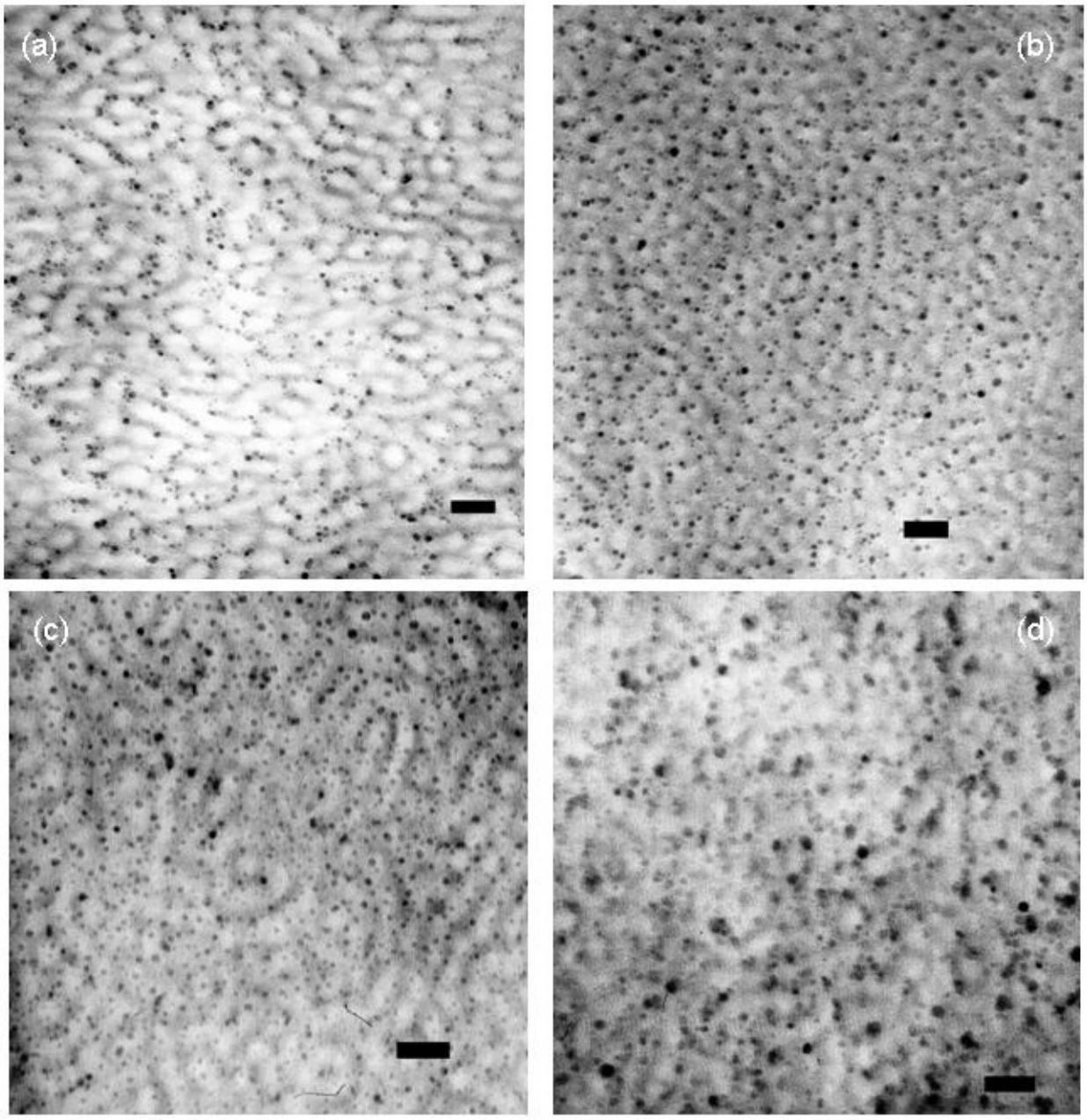

Figure 2.7: TEM images of crosslinked S-SEBS doped with different Ti/SO_3H molar ratios. (a)0.02, (b)0.04, (c)0.16, (d)0.32. (scale bar = 50 nm)

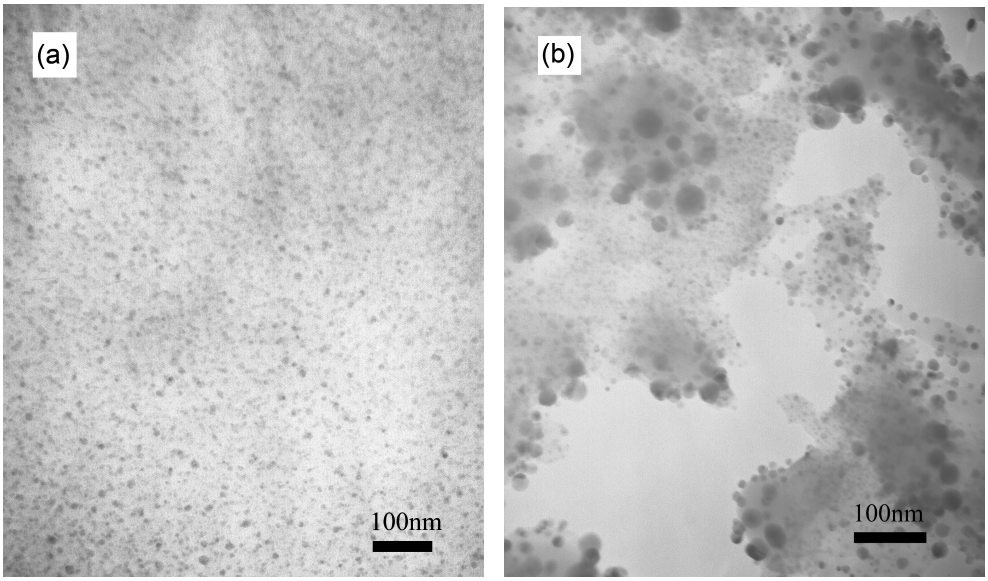

Figure 2.8: TEM images of crosslinked S-SEBS doped with different Ti/SO_3H molar ratios: (a)0.48, and (b)0.64.

2.3.3 Mechanical Properties of TiO_2 Composites with Crosslinker

Dynamic mechanical experiments were used to evaluate the tensile strength and ultimate elongation of the S-SEBS composites containing titanium dioxide nanoparticles and crosslinker. Controlled force stress/strain experiments were performed to obtain the stress-strain curve shown in Figure 2.9. Compared to the pure S-SEBS block copolymer, the ultimate elongation of the composites was smaller, however the tensile strength was larger. The glass transition temperatures of the nanocomposites were determined by a controlled strain (0.1%) temperature ramp experiment (frequency set at 1 Hz and heating rate was 7 $^{\circ}C$/min), as shown in Figure 2.10. The glass transition temperature of [ethylene-ran-butylene] blocks was not significantly affected by the doped TiO_2 nanoparticles and crosslinker, only shifting to 3 $^{\circ}C$ higher for all the composites. This indicated that nanoparticles and

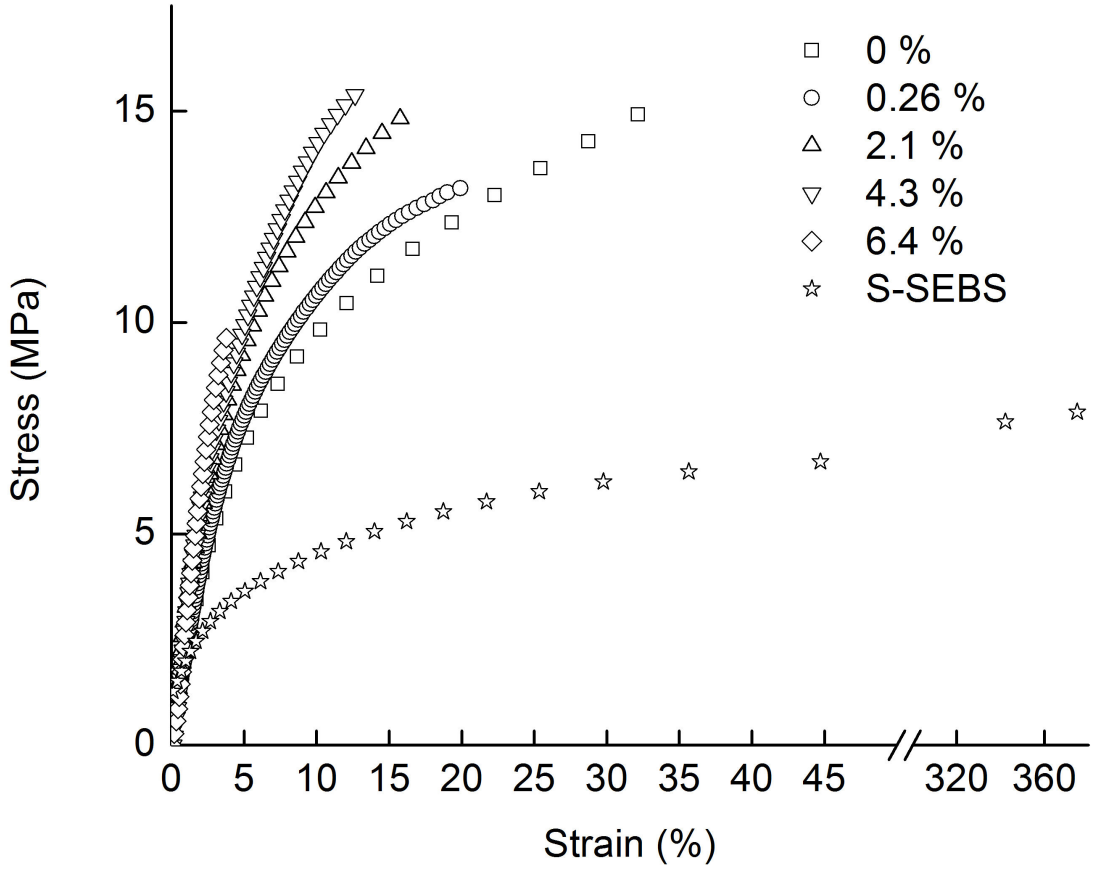

Figure 2.9: Mechanical stress/strain curves of S-SEBS composites with different TiO_2 wt%. Molar ratio of crosslinker/SO_3H = 2.5.

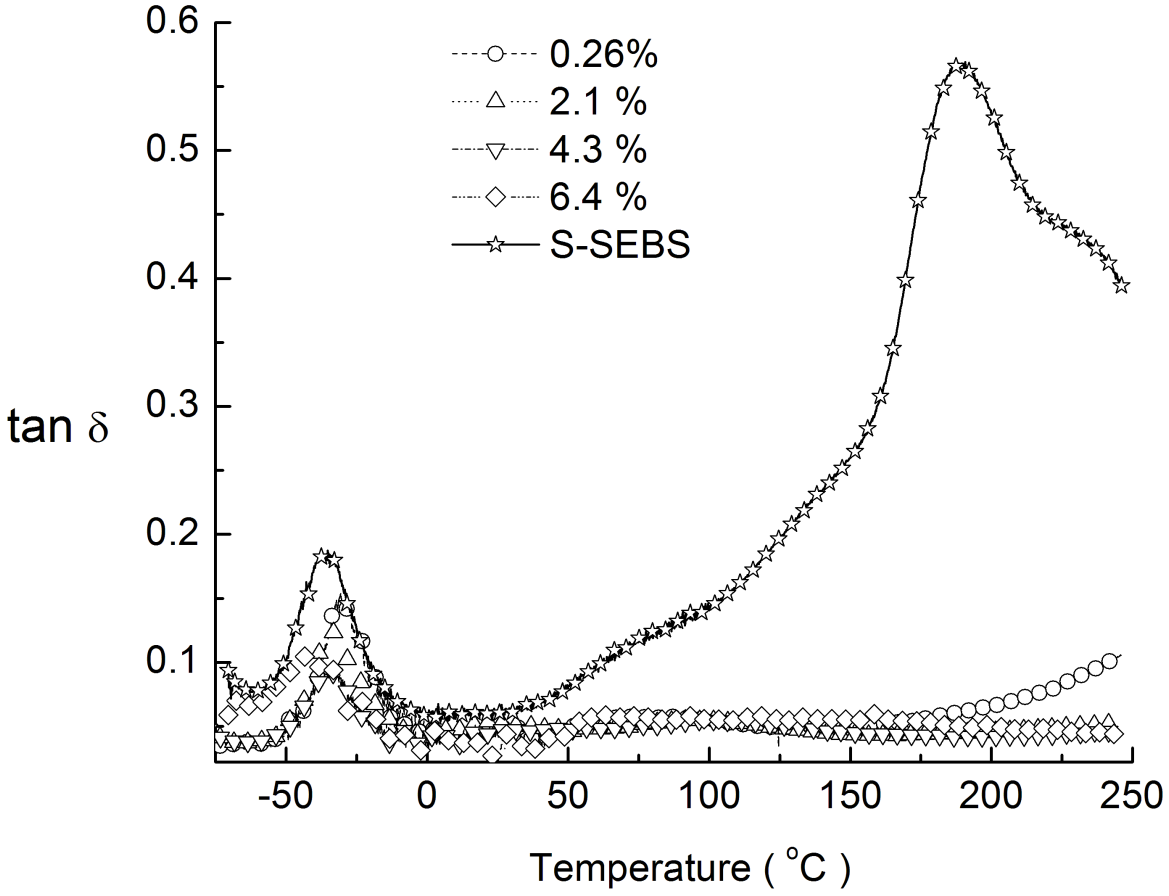

Figure 2.10: Mechanical loss tangent of S-SEBS composites with different TiO_2 wt%. Molar ratio of crosslinker/SO_3H = 2.5.

crosslinker were both confined within the sulfonated styrene blocks and had no effect on the chain relaxation behavior of the rubbery [ethylene-ran-butylene] blocks. However, upon crosslinking the glass transition temperature of the sulfonated styrene blocks was suppressed compared to the broad peak between 50 and 250 $^{\circ}C$ of the pure S-SEBS copolymer. It has been reported in literature that the relaxation peak of the composites becomes broader and shifts to higher temperatures with increasing crosslink density or addition of particles [89, 90]. Since the nanocomposites consist of only up to 6.4 wt% of TiO_2 particles, the suppressed transition temperature could be attributed to the crosslinked sulfonated styrene groups resulting from addition of crosslinker and sulfone group formation. The TGA data (Figure 2.11) show that the weight loss for the pure S-SEBS block copolymer was higher with increasing temperature compared to the temperature-stable S-SEBS with crosslinker (up to 300 $^{\circ}C$). For the un-crosslinked S-SEBS, the weight loss contributes to water evaporation below 100 $^{\circ}C$. The sulfonic acid groups are eliminated to form sulfone (RSO_2R) groups at temperatures higher than 100 $^{\circ}C$ [91, 92, 93].

The crosslinked nanocomposites containing confined TiO_2 nanoparticles also led to higher tensile strength and less ultimate elongation compared to un-crosslinked S-SEBS, as shown in Figure 2.9.

2.3.4 Swelling Tests

Swelling experiments were performed to demonstrate the absence of sulfonic acid groups in the crosslinked composites. Three different polymers were tested:

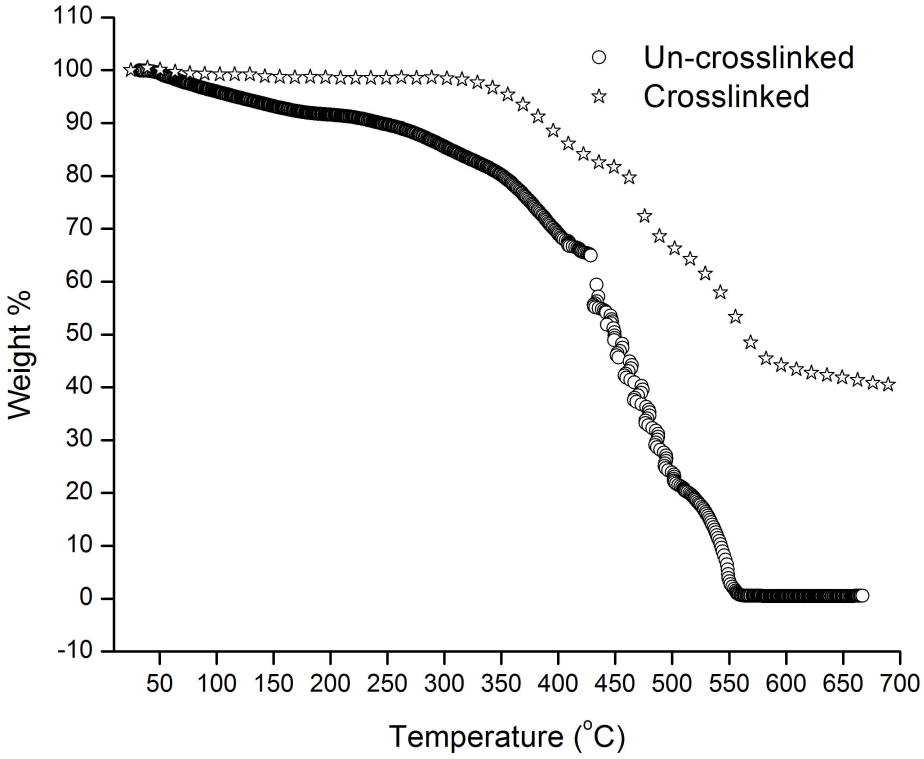

Figure 2.11: TGA curves for pure S-SEBS and S-SEBS with crosslinker. Molar ratio of crosslinker/SO_3H = 2.5.

1. Block copolymer of [styrene-b-(ethylene-ran-butylene)-b-styrene] (SEBS) with 28 wt% styrene.

2. Block copolymer of [sulfonated styrene-b-(ethylene-ran-butylene)-b-styrene] (S-SEBS) with 29 wt% styrene and 59.7 mol% of styrene sulfonated.

3. S-SEBS block copolymer with crosslinker [Molar ratio of crosslinker/SO_3H = 2.5].

The swelling ratio (q) was calculated, as $q = W_a/W_0$, where W_a is the weight of the film swollen by water to equilibrium and W_0 is the weight after drying. The results shown in Figure 2.12 demonstrate that the swelling ratio for the SEBS copolymer without any strong SO_3H polar groups was 1, which means water cannot penetrate into the polymer. In contrast, the S-SEBS block copolymer exhibited significant swelling ($q = 4$) due to the highly hydrophilic sulfonic acid groups on the sulfonated styrene blocks. For the S-SEBS block copolymer with crosslinker, the swelling ratio dropped back to 1. This experiment qualitatively indicated that the hydrophilic sulfonic groups were eliminated to form the sulfone crosslinks or were replaced by the hydrophobic silane groups of the crosslinker.

2.3.5 Dielectric Properties of S-SEBS Block Copolymer TiO_2 Composites

The dielectric permittivity of a material is usually given relative to that of free space, and is known as relative permittivity (ε_r), or dielectric constant (k).

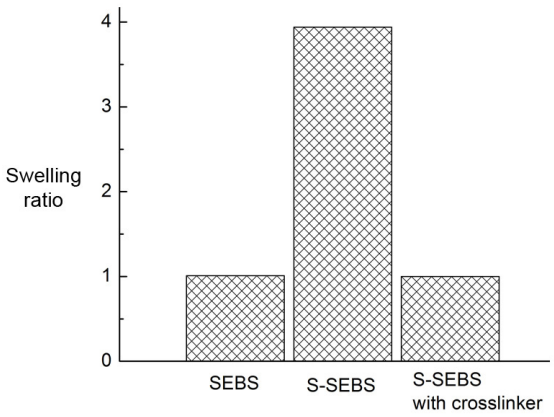

Figure 2.12: Swelling ratios for various S-SEBS block copolymers.

The dielectric response of the nanoparticle composites at various frequencies is described in terms of the complex permittivity (ε^*) which is represented by its real and imaginary parts.

$$\varepsilon^* = \varepsilon' - i\varepsilon'' \tag{2.1}$$

where ε' is the dielectric permittivity and ε'' is the dielectric loss. The dielectric loss tangent ($\tan\delta$) is defined as

$$\tan\delta \equiv \frac{\varepsilon''}{\varepsilon'} \tag{2.2}$$

The dielectric data obtained from the pure (un-crosslinked) S-SEBS block copolymer suggested that this polymer was a lossy material, which means the charges dissipated are comparable to those stored within S-SEBS and not favorable for dielectric material applications. For example, the dielectric loss tangent of pure S-SEBS was 0.6 while the relative permittivity was 5258 at a frequency as of 10 kHz, as shown in Figure 2.13. The reason for the prominent loss was contributed to

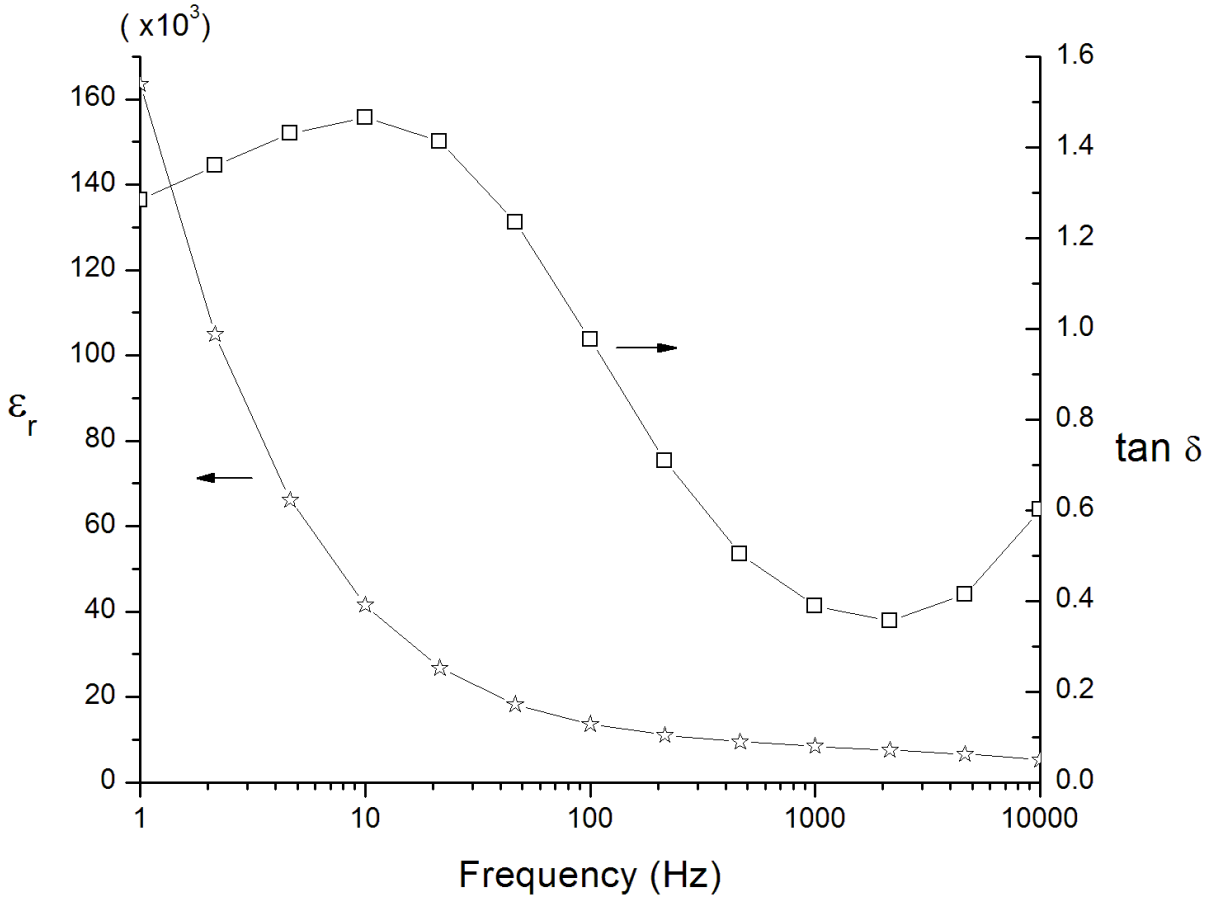

Figure 2.13: Dielectric properties of un-crosslinked pure S-SEBS copolymer.

the strong proton/charge conducting ability of the SO_3H groups on the sulfonated styrene blocks, leading to the dissipation of the charges within the S-SEBS [94]. In order to reduce the dielectric loss resulting from the mobile protons in the sulfonic acid groups, crosslinkers were introduced into the sulfonated styrene blocks to replace the protons. The resulting S-SEBS/crosslinker composite, where the molar ratio of crossliner to SO_3H groups was 2.5, showed that the dielectric loss tangent was suppressed below 0.01 at 10 kHz as well as for the composites with various amounts of TiO_2 nanoparticles (see Figure 2.14b). The data also showed that dielectric loss decreased with increasing amount of nanoparticles which can be due to the strong polar SO_3H groups being replaced by the crosslinker and the mobility of polymer chains being hindered by the nanoparticles and crosslinker. The data obtained also show that the relative permittivity of the composites increases by doping TiO_2 nanoparticles: the higher the amount doped, the higher the permittivity obtained as shown in Figure 2.14a.

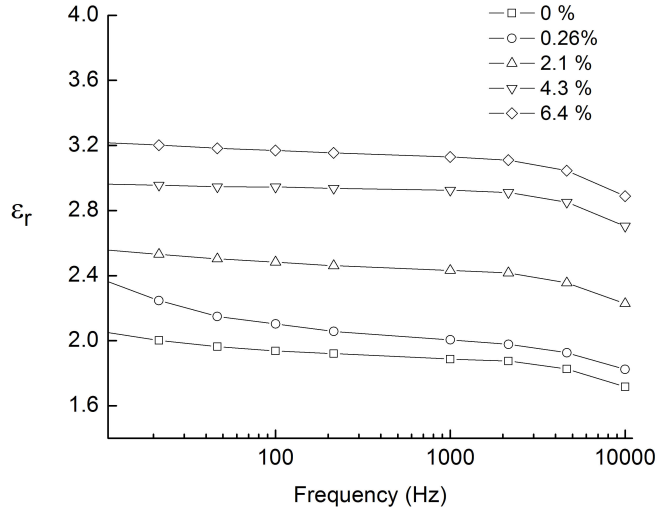

(a) Relative permittivity

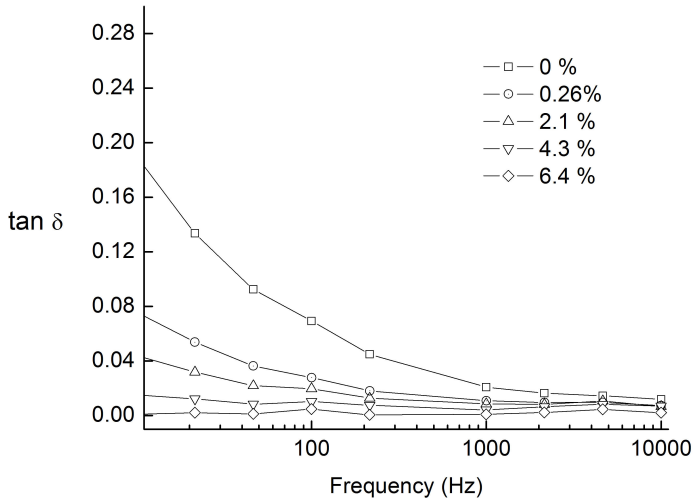

(b) Dielectric Loss Tangent

Figure 2.14: Dielectric properties for S-SEBS with different TiO_2 wt%. Molar ratio of crosslinker/SO_3H = 2.5.

2.4 Conclusions

The feasibility of producing high dielectric permittivity nanoparticles (TiO_2) uniformly dispersed within polymer matrices has been shown. The self-assembled morphologies of block copolymers enable the formation of TiO_2 nanoparticles well dispersed within the sulfonated styrene domains throughout the entire sample. In addition, both TiO_2 nanoparticles and crosslinks could be simultaneously formed within the sulfonated styrene block while maintaining the original block copolymer microphase separation. Dielectric experiments showed that higher permittivity composites can thus be obtained with a significant decrease in loss $\tan\delta$ (<0.01) when crosslinked with vinyltrimethoxysilane.

Chapter 3

Magneto-dielectric Properties of Polymer-Ferrite Nanocomposites

3.1 Introduction

In this study, we investigated the magnetic particle characteristic length effect on the resultant polymer composites' magneto-dielectric properties in order to obtain high ε_r and μ_r composites with low loss. Various domain wall structure ferrites including soft and hard ferrites with/without multi-domain walls were utilized to elucidate the effect of domain wall movement on the resultant values of μ_r when materials were subjected to alternating magnetic field. The composites' magneto-dielectric properties influenced by thermal energy fluctuation (superparamagnetism effect) were also investigated using surface-modified magnetic nanoparticles. Surface-modified iron oxide (Fe_3O_4) and nickel zinc ferrite ($NiZnFe_2O_4$) nanoparticles were synthesized using a sodium oleate surfactant to improve compatibility with the polymer matrix. The size of the nanoparticles was tailored by a seed-mediated method, which utilizes smaller nanoparticles as growth sites to syn-

thesize larger particles. A possible mechanism for the nucleation and growth of nanoparticles will be discussed. The dielectric (ε_r) and magnetic (μ_r) properties of the resulting nanocomposites consisting of various particles dispersed in polymer matrices were measured at radio frequencies (1 M to 1 GHz).

3.2 Experimental Section

Materials: Sodium oleate (97%) was purchased from TCI America. Iron(III) chloride (97%), oleic acid (90%),1-octadecene (90%), nickel zinc iron oxide ($NiZnFe_2O_4$, <50nm), strontium ferrite ($SrFe_{12}O_{19}$, <50nm), iron oxide(Fe_3O_4, <50nm) were purchased from Aldrich. Isometric and acicular iron oxide (Fe_3O_4) were supplied by BASF and Cathay Pigments, respectively. The block copolymer of [styrene-b-ethylene/butylene-b-styrene] (SEBS) was supplied by Kraton Polymers. All chemicals were used as received.

Synthesis of 11 nm Fe_3O_4 nanoparticle seeds: The procedure for synthesizing the surfactant-modified iron oxide nanoparticles is similar to what has been reported in literature [29]. $FeCl_3$ (10.8 g) and sodium oleate (36.5 g) were reacted in a mixed solvent (80 ml ethanol, 60 ml distilled water and 140 ml hexane) at 70 $^\circ C$ for 4 hours. The upper organic layer containing the iron-oleate complex (Fe precursor) was washed three times with 30 ml distilled water and then dried. The resulting iron-oleate complex was added to 200 mL of 1-octadecene mixed with oleic acid (5.7 g). The mixture was heated to 320 $^\circ C$ in an argon atmosphere. After 30 minutes at 320 $^\circ C$, the solution turned black and was then cooled down to room temperature.

Ethanol was added to precipitate the surfactant-coated iron oxide particles. The precipitated particles were centrifuged to remove any residual solvents.

Synthesis of Fe_3O_4 nanoparticles via 11 nm (Fe_3O_4) seeds: The 11 nm Fe_3O_4 nanoparticles were used as growth seeds to obtain larger particles. The amounts of iron-oleate complex (Fe precursor), oleic acid, and seeds were systematically varied and their effect on resulting nanoparticle size was studied. All components were added into a solvent (1-octadecene) and heated to 320 $°C$ for 3 hours. After cooling to room temperature and adding excess ethanol, surfactant-coated iron oxide particles were recovered from solvent.

Synthesis of 13.2±3.8 nm $NiZnFe_2O_4$ nanoparticle seeds: $FeCl_3$ (3.89 g), $NiCl_2$ (0.78 g), $ZnCl_2$ (0.82 g) and sodium oleate (29.2 g) were reacted in a mixed solvent (80 ml ethanol, 60 ml distilled water and 140 ml hexane) at 70 $°C$ for 4 hours. The upper organic layer containing the metal-oleate complex ($NiZnFe$ precursor) was washed three times with 30 ml distilled water and then dried. The resulting complex was added into 200 mL of 1-octadecene mixed with oleic acid (5.6 g). The mixture was heated to 320 $°C$ in an argon atmosphere. After 30 minute at 320 $°C$, the solution turned black and was then cooled down to room temperature. Ethanol was added to precipitate the surfactant-coated nickel zinc iron oxide ($NiZnFe_2O_4$) particles. The precipitated particles were centrifuged to remove any residual solvents.

Synthesis of 17.3±5.6 nm $NiZnFe_2O_4$ nanoparticles via seeds: The procedure was the same as with the synthesis of 13.2±3.8 nm $NiZnFe_2O_4$ seeds except the addition of 2g 13.2±3.8 nm seeds to obtain lager particles.

Synthesis of 16.1±9.2 nm $NiZnFe_2O_4$ nanoparticles via seeds: The procedure was the same as with the synthesis of 13.2±3.8 nm $NiZnFe_2O_4$ seeds except the addition of 2g 17.3±5.6 nm nanoparticles as growth seeds to synthesize nanoparticles.

Preparation of Fe_3O_4 nanocomposites: Fe_3O_4/polymer nanocomposites were prepared using a solution-casting method, since both surfactant-modified Fe_3O_4 and polymer dissolve in a common solvent, tetrahydrofuran (THF). The modified Fe_3O_4 particles and polymer (SEBS) were dissolved in THF and mixed for 1 hour, then a film was static cast over a period of one day.

Preparation of $Ni_{0.5}Zn_{0.5}Fe_2O_4$ nanocomposites: The $Ni_{0.5}Zn_{0.5}Fe_2O_4$ / polymer nanocomposites were prepared by a solution-casting method since both surfactant-modified $Ni_{0.5}Zn_{0.5}Fe_2O_4$ and polymer dissolve in a common solvent, tetrahydrofuran (THF). The modified-Fe_3O_4 particles and polymer (SEBS) were mixed in THF solution for 1 hr, and a film was cast over a period of one day.

Characterization: Transmission electron microscopy (TEM, HITACHI H-600 or JEOL 200CX) was used to observe the morphology of the nanoparticles. Samples for TEM were prepared by evaporating a dilute Fe_3O_4 THF solution on a carbon-coated grid. The particle size is reported as the average size (D_{avg}), which is the average particle size of approximately 1000 individual particles from TEM images. Magnetic properties were investigated using superconducting quantum interference device (SQUID) magnetometry. Samples for SQUID measurements consisted of approximate 10 wt% of iron oxide particles and their weight were in the 15 mg range. The form of the samples was cubic geometry (2mm x 2mm x 2mm). The

amount of iron oxide inside the polymer matrix was determined using thermogravimetric analysis (TGA-50, SHIMADZU) in nitrogen atmosphere. The polymer and surfactant were burnt out and only iron oxide particles remained without change in the crystalline structure. The magneto-dielectric properties (relative dielectric permittivity, ε_r, and relative magnetic permeability, μ_r) in the 1MHz to 1GHz range were measured using an Agilent RF impedance/material analyzer (E4991A). Samples for ε_r measurement were prepared in the shape of a solid disc with a diameter of 0.75 inch and a thickness of 0.1 inch. Samples for μ_r measurement were in the geometry of a washer with an outer diameter of 0.75 inch, an empty inner diameter of 0.25 inch, and a thickness of 0.1 inch.

3.3 Results and Discussion

3.3.1 Effect of Particles' Magnetic Domain Wall Movement on Polymer Composites' Magneto-dielectric Properties

3.3.1.1 Effect of coercive field and conductivity of particles on composites' magneto-dielectric properties

Commercial strontium ferrite ($SrFe_{12}O_{19}$), nickel zinc ferrite ($NiZnFe_2O_4$), and iron oxide (Fe_3O_4) nanoparticles were used to investigate the hysteresis effect of magnetic materials subjected to an alternating magnetic field. The coercivities of $SrFe_{12}O_{19}$, Fe_3O_4 and $NiZnFe_2O_4$ are in the order of 4 kOe [95, 96], 0.2 kOe [97],

and 20 Oe [43], respectively. Large coercivity ferrites (hard ferrites) do not instantaneously follow the external alternating field due to the difficulty of moving their domain walls. Low coercivity ferrites (soft ferrites) were easy to move domain walls in response to a changing magnetic field. In the 1MHz to 1GHz, the SEBS polymer composites with both $NiZnFe_2O_4$ and Fe_3O_4 (soft ferrites) exhibited larger values of μ_r than with $SrFe_{12}O_{19}$ (hard ferrite) nanoparticles, shown in Figure 3.1. The 46 wt% $SrFe_{12}O_{19}$ hard ferrite composite with a value of μ_r near 1 indicated that the internal magnetization can not instantaneously follow the alternating field, resulting in a low value of μ_r. The Fe_3O_4 composite showed the highest value of ε_r among the three composites, shown in Figure 3.2. However, it also showed highest dielectric loss, which is not a desired property for microwave communication application.

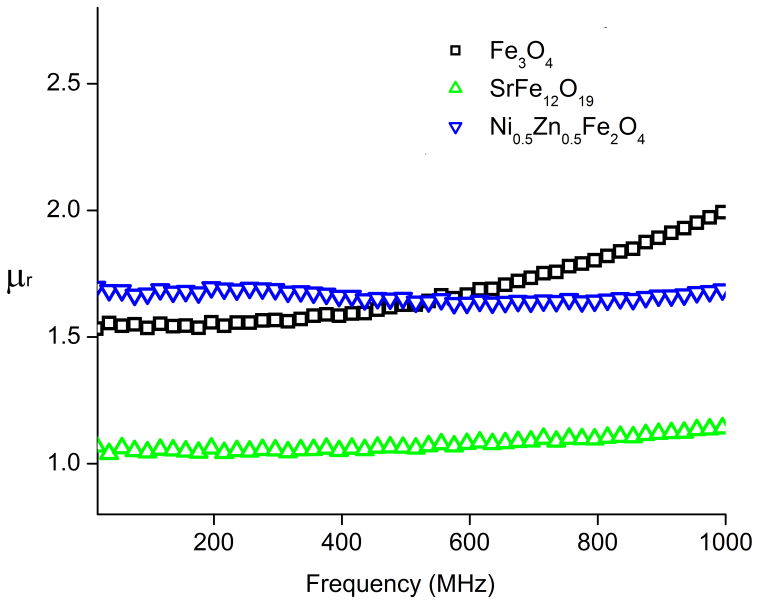

Figure 3.1: Magnetic permeabilities of polymer composites with 46 wt% soft and hard ferrites.

The relative dielectric permittivity and magnetic permeability of the poly-

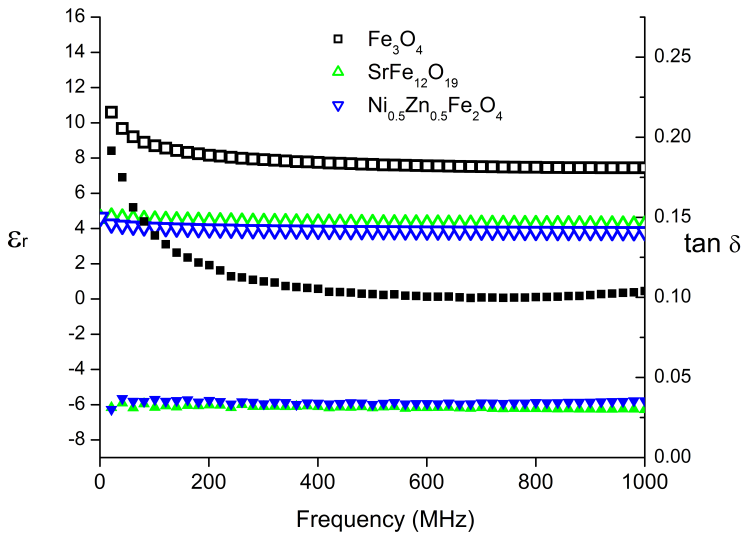

Figure 3.2: Dielectric permittivity (ε_r, empty symbols) and loss (tanδ, solid symbols) of polymer composites with 46 wt% soft and hard ferrites.

mer nanocomposites with commercial $NiZnFe_2O_4$ nanoparticles are shown in Figures 3.3. The relative permittivity of the SEBS copolymer ($\varepsilon_r = 2.4$) improved from 2.4 to 4.7 with increasing amount of $NiZnFe_2O_4$ nanoparticles while the dielectric loss (tanδ) increased as well (Figure 3.4). The magnetic permeability of the SEBS copolymer (μ_r= 1) also improved from 1.0 to 2 at 1 GHz with increasing amount of $NiZnFe_2O_4$ nanoparticle doping.

3.3.1.2 Magnetic multi-domain effect on the composite's magnetic permeability

Fe_3O_4 particles with various characteristic lengths were utilized to investigate the effect of magnetic domain walls on μ_r of composites. The TEM images of the particles (Figure 3.5) used for these composites showed that the particle sizes of

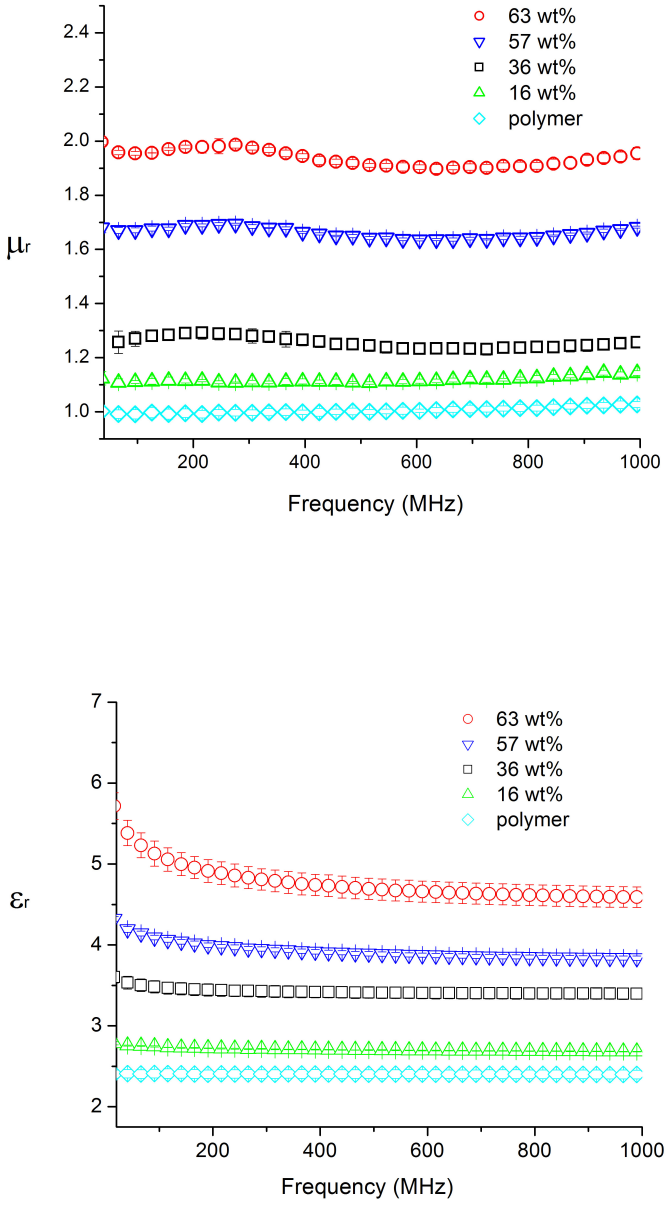

Figure 3.3: High frequency relative permittivity (ε_r) and magnetic permeability (μ_r) of commercial $NiZnFe_2O_4$ nanocomposites at room temperature.

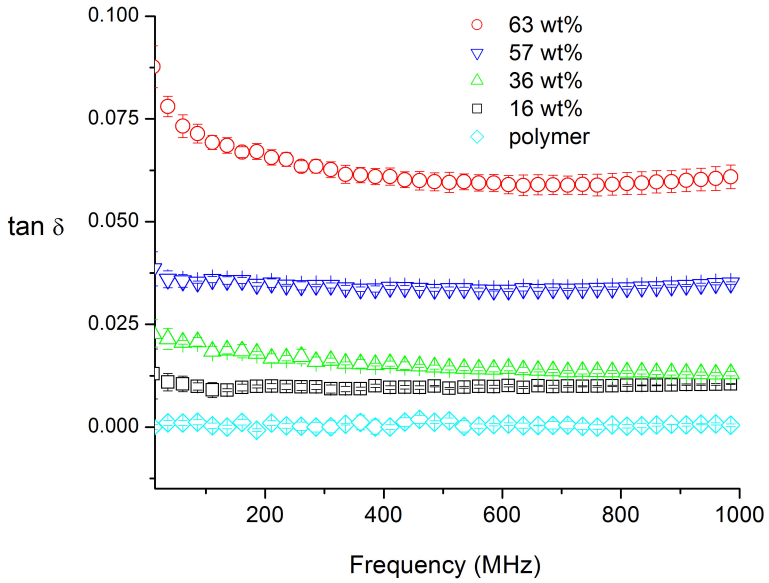

Figure 3.4: Dielectric loss (tanδ) of commercial $NiZnFe_2O_4$ nanocomposites at high frequency range.

isometric and acicular particles are above the 50-60 nm critical limit (D_{SD}) for single magnetic domains [98]. This means that these particles consist of magnetic multi-domains . The resulting magnetic permeability of polymer composites with 57 wt% particles showed that particles with magnetic multi-domains have an adverse affect on the values of μ_r (Figure 3.6). The composites with the single-domain or superparamagnetic nanoparticles (Figure 3.5a) showed higher values of μ_r than with multi-domain particles. Moving more domain walls in response to an alternating magnetic field led to less magnetization and a lower measured μ_r value.

3.3.1.3 Conclusions

Polymer composites consisting of low coercivity soft ferrites (Fe_3O_4 and $NiZnFe_2O_4$) showed high μ_r due to the ability to move domain walls easily in response to an alter-

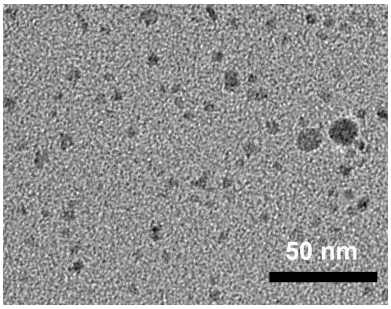

(a) Nanoparticles

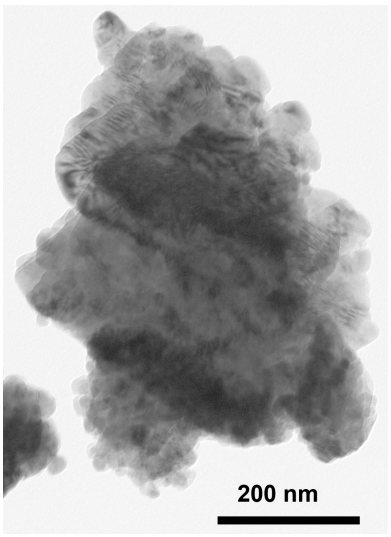

(b) Isometric particles

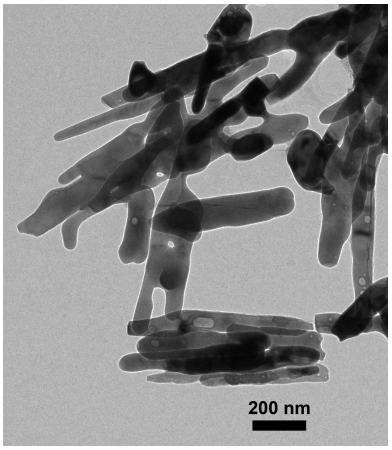

(c) Acicular particles

Figure 3.5: TEM images of Fe_3O_4 with various characteristic lengths

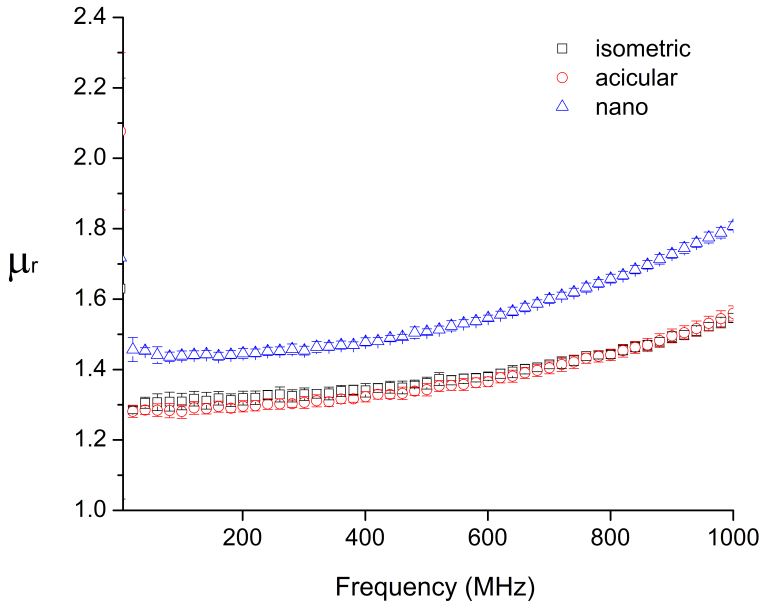

Figure 3.6: Magnetic permeabilities of polymer composites with 57 wt% various characteristic length Fe_3O_4 particles.

nating magnetic field. However, Fe_3O_4 exhibited higher dielectric loss (tan δ) due to intrinsic high electrical conductivity. Magnetic particles with magnetic multi-domains (size larger than approximately 100 nm), have low permeabilities at 1 GHz range due to magnetic domain wall movement. When such magnetic particles are subject to a magnetic field, their magnetic domain walls move their boundaries to align with the direction of applied field. More domain wall movement results in decreased ability to quickly respond to an applied alternating field (GHz), thus leading to lower magnetization and magnetic permeability.

3.3.2 Surface-modified Fe_3O_4 Nanocomposites

Surface-modified Fe_3O_4 nanoparticles were utilized to elucidate the characteristic length affect on the resultant magnetic properties given their well-defined shapes and sizes [29, 99]. However, such nanoparticles are too small so that they are superparamagnetic, which no magnetic domains present within the nanoparticle. In order to investigate how magnetic domain walls affect resultant magnetic properties, a seed-mediated growth method was utilized to synthesize larger nanoparticles with magnetic domain wall present.

3.3.2.1 Structural characterization of surface-modified Fe_3O_4 seeds

The nanoparticle seeds used in the seed-mediated growth studies were spherical with narrow size distribution, as shown in Figure 3.7. The lattice fringes of an isolated particle obtained by high resolution TEM indicates that the particle is a single crystal (Figure 3.8). The average size (D_{avg}) measured from TEM was 11.3±0.3 nm. Figure 3.9 depicts a selected area electron diffraction pattern from the synthesized nanoparticles in Figure 3.7a and shows multiple diffraction rings. The calculated lattice d-spacings derived from the diffraction rings is consistent with bulk or nano-size magnetite (Fe_3O_4) reported in literature [64, 100], as shown in Table 3.1. The chemical composition of Fe_3O_4 was also confirmed by comparing the properties of as-synthesized particles and their heat-transformed form, γ-Fe_2O_3. However, the majority of the synthesized nanoparticle composition should be Fe_3O_4

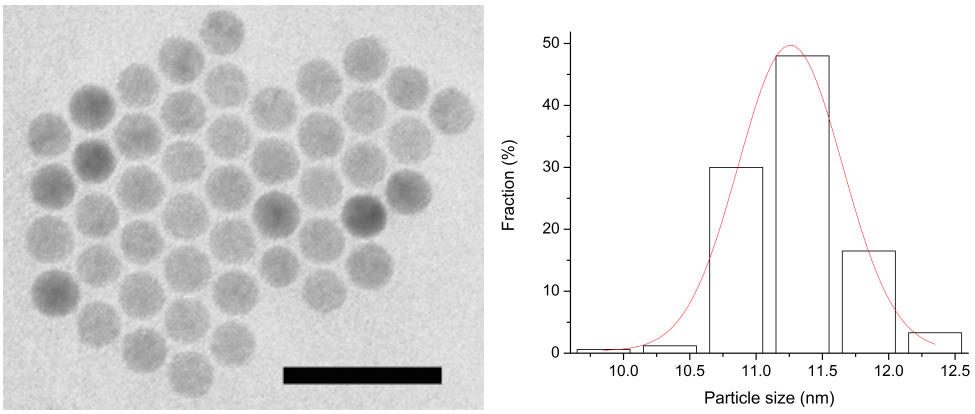

(a) TEM image.

(b) Particle size distribution.

Figure 3.7: TEM image of surfactant-modified Fe_3O_4 nanoparticles (scale bar = 50 nm).

with a small percentage of γ-Fe_2O_3, as reported in literature [29].

Ring	1	2	3	4	5	6	7
d	4.85	2.98	2.53	2.10	1.72	1.62	1.50
hkl	111	220	311	400	422	511	440

Table 3.1: Lattice spacing of Fe_3O_4, d(Å), derived from the diffraction pattern shown in Figure 3.9.

3.3.2.2 Mechanism of Fe_3O_4 formation by seed-mediated growth

In the classic LaMer mechanism [101], the formation of colloids from homogenous solution occurs when the precursor concentration is above the supersaturated limit. This means that the probability of particle precursors encountering each other

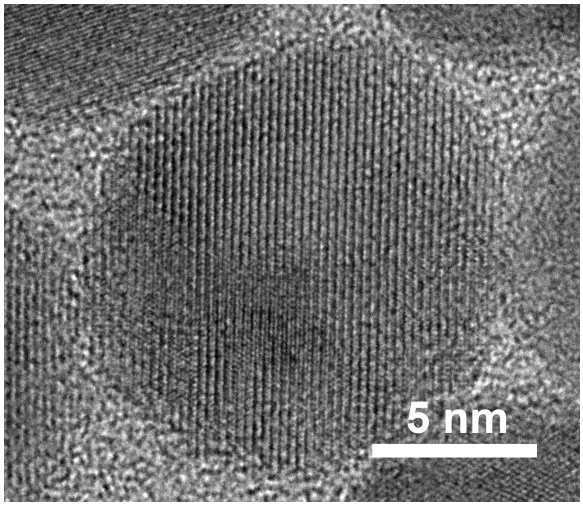

Figure 3.8: High resolution TEM image of a single Fe_3O_4 nanoparticle.

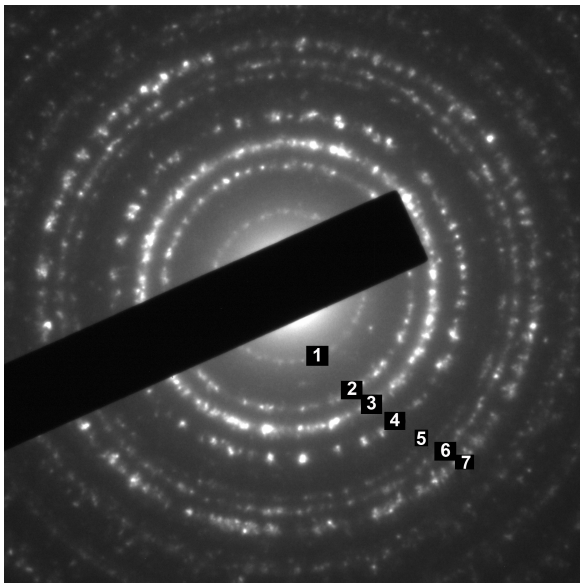

Figure 3.9: Selected area electron diffraction pattern of Fe_3O_4 nanoparticles.

is sufficiently high, resulting in nanoparticle nucleation. Further growth of the nuclei is spontaneous but limited by diffusion of the precursor to the nucleus surface. In our nanoparticle synthesis system, iron ions were released by dissociation from the iron-oleate complex at 320 $°C$ [29]. When the concentration of Fe^{3+} ions in solution overcomes the supersaturation limit, Fe_3O_4 particle nucleation takes place and subsequently the nuclei grow to larger particles. However, the particles stopped growing and stabilized at an approximate size of 11 nm within 30 minutes at 320 $°C$ [29]. Even though the reaction was continued for 10 hours, no particle growth was observed by Ostwald ripening [65]. Therefore, the seed-mediated method was utilized in order to obtain larger particles. This method has been applied to the growth of metal oxides or multi-metallic nanoclusters [64, 102]. In our study, the synthesized Fe_3O_4 nanoparticle seeds were used as nuclei to grow larger Fe_3O_4 particles. The key factors affecting Fe_3O_4 particle homogenous nucleation from solution, and growth from seed particle nuclei surface were Fe precursor (iron-oleate complex), surfactant (oleic acid), and seed size [65, 103, 104]. The experimental results reported for sample 1 to 7 studied the surfactant/precursor effect and sample 8 was used to investigate the seed size effect.

Surfactant & Fe precursor: Sample 1 indicated that Fe_3O_4 nanoparticles did not grow to a larger size as expected by the amount of seeds added, when the concentration ratio of oleic acid surfactant to Fe precursor (S/Fe) was 2 and 3.2 g/L of seeds was used (see Table 3.2 and Figure 3.10).

The same particle distribution between sample 1 and 2 also indicates that the Fe_3O_4 nucleation rate from solution was faster than the nuclei growth rate

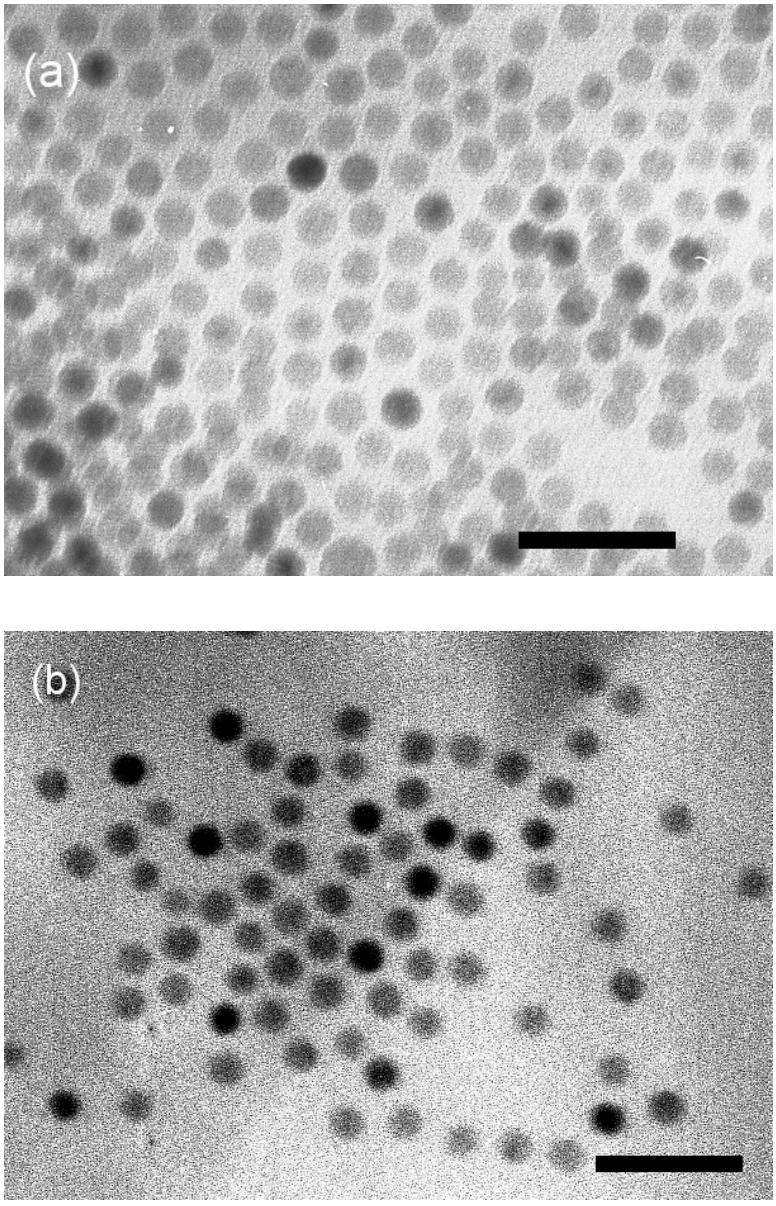

Figure 3.10: TEM images of high S/Fe nanoparticles: (a) sample 1 and (b) sample 2 (scale bar = 50nm).

Sample	S/Fe	$[seed]$ (g/L)	D_{avg} (nm)
Seed	0.5	0	11.3±0.3
1	2	3.2	10.1±0.6
2	2	7.9	9.8±0.8
3	4	3.2	0

Table 3.2: Effect of surfactant concentration on average particle size (D_{avg}).

Sample	S/Fe	$[seed]$ (g/L)	D_{avg} (nm)
4	1	7.9	18.4±2.1
5	0.5	7.9	22.2±4.5
6	0.25	7.9	13.9±1.7
7	0	7.9	10.1±2.1

Table 3.3: Effect of surfactant concentration on average particle size (D_{avg}).

although the seed concentration was doubled when the S/Fe ratio was kept at 2. At higher surfactant concentration (S/Fe=4), no Fe_3O_4 particles were formed, which is consistent with literature reports that excess surfactant impedes the formation of Fe_3O_4 particles [65, 104]. As the ratio S/Fe decreased from 2 to 0.5, the average particle size (D_{avg}) increased as shown in Figure 3.11 and Table 3.3.

However, D_{avg} decreased again at a ratio S/Fe of 0.25 (sample 6 in Table 3.3). These results suggest that extremely low surfactant concentrations have an adverse

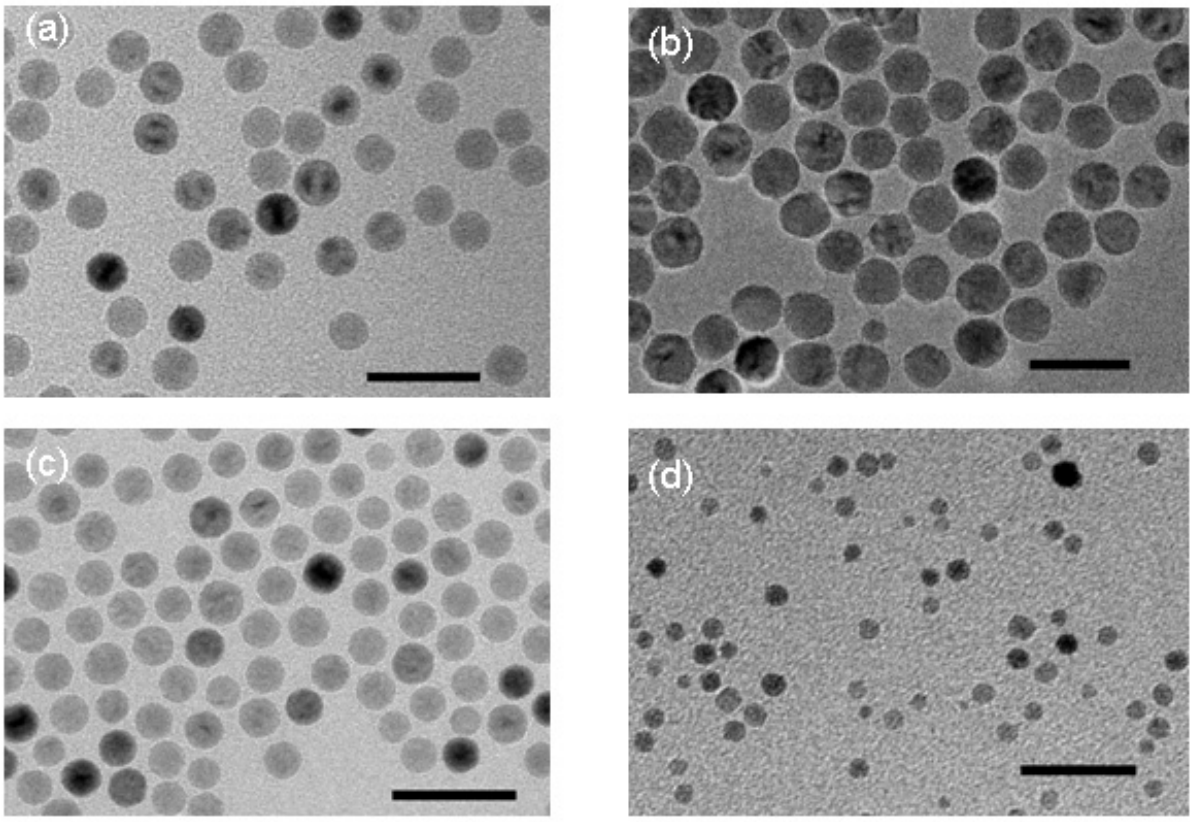

Figure 3.11: TEM images of low S/Fe nanoparticles: (a)sample 4; (b)sample 5; (c)sample 6; and (d)sample 7 (scale bar = 50nm).

effect on particle growth from nuclei although modest surfactant present in solution promotes Fe_3O_4 formation in favor of particle growth. To further investigate the effect of less surfactant on nanoparticle growth, the particle synthesis was conducted without adding surfactant (sample 7 in Table 3.3). In addition, an excess of oleylamine was added into the solution in order to reduce the reactivity of oleate surfactant present in the Fe precursor and seeds. It is well-known that carboxylic acid ($-COOH$) groups of oleate-surfactants tend to associate with amine groups ($-NH_2$) of oleylamine instead of associating with the Fe^{3+} ions or the Fe_3O_4 nanoparticle surface [28, 105]. The observed D_{avg} of 10.1 nm with high standard deviation ($\pm$2.1 nm) confirms that less surfactant leads to formation of smaller particles (Figure 3.11d). Overall, the effect of the ratio S/Fe on particle size distribution can be summarized in Figure 3.12.

The optimal ratio (S/Fe) is 0.5 for growing larger particles. Two distinct regions can be found in which the particle size decreases with decreasing (Region I) or increasing S/Fe (Region II), respectively. These results can be explained by the free Fe^{3+} ions present in the solution (Fe_{free}). Fe_{free} is the amount of Fe^{3+} ions not associated (trapped) by surfactants, which freely participates in Fe_3O_4 formation. In Region I, less surfactant or more iron precursor (lower S/Fe) results in higher Fe_{free} to overcome the supersaturation limit for nucleating Fe_3O_4 nanoparticles from homogeneous solution. Fe_{free} ions were consumed for nucleating small particles (nucleation domination) instead of diffusing to nuclei for nanoparticle growth as shown in Figure 3.13.

In Region II, Fe_3O_4 nucleation dominated with increased $R_{S/Fe}$. As shown

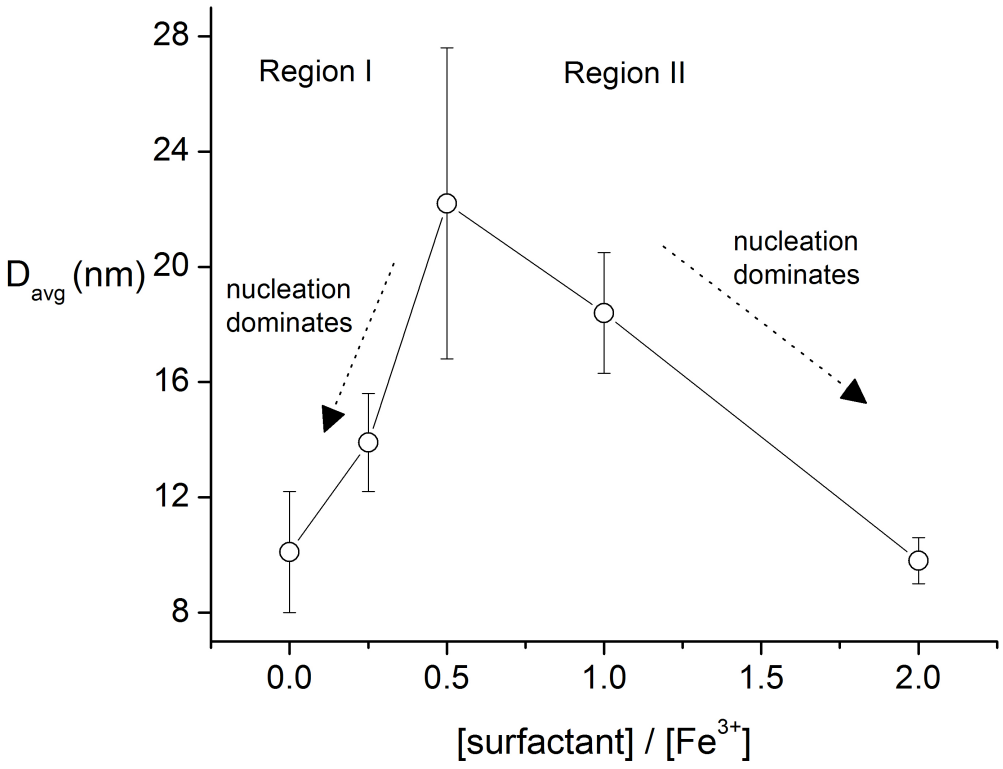

Figure 3.12: Effect of S/Fe on Fe_3O_4 particle size distribution

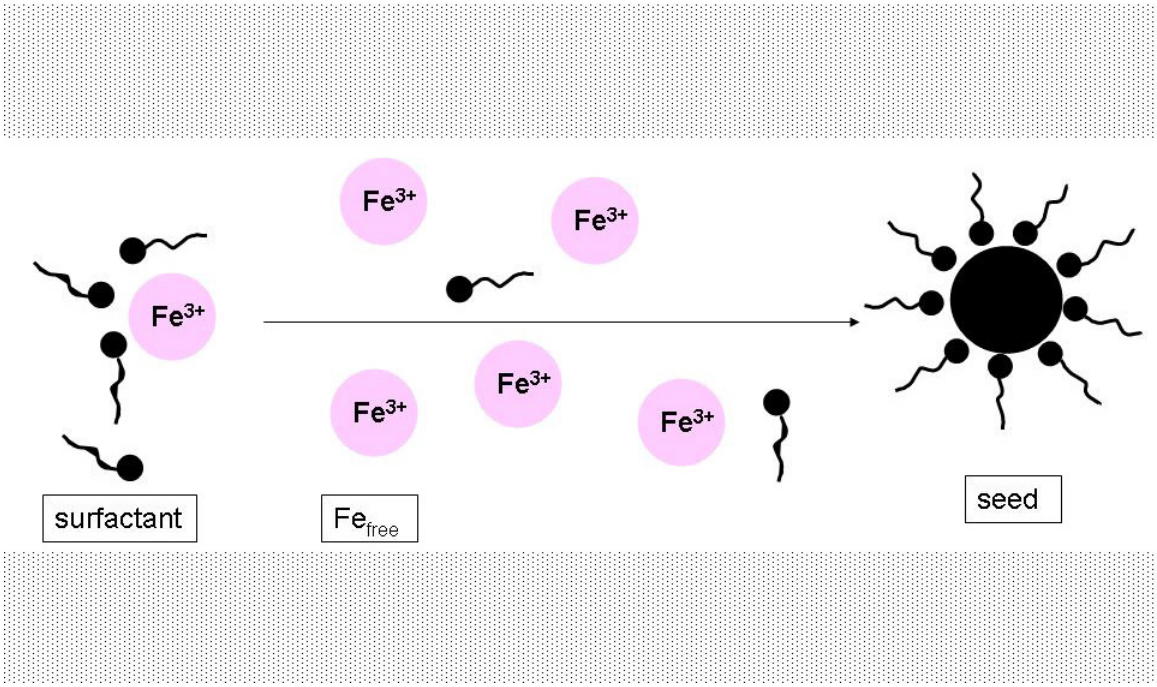

Figure 3.13: Effect of low S/Fe on Fe_3O_4 nanoparticle formation

in Figure 3.14, once Fe_{free} ions were released from the iron-oleate complex, they re-associated with surfactants already present in the solution.

Therefore, higher surfactant concentrations promoted Fe_{free} ion localization and hindered their diffusion into stable nuclei for particle growth. Consequently, Fe_3O_4 nucleated to smaller nuclei instead of growing to larger particle sizes. No Fe_3O_4 nanoparticles formed, because most Fe_{free} ions were captured at extremely high surfactant concentration (sample 3 in Table 3.2).

Seed size: The seed size effect on Fe_3O_4 nanoparticle formation was studied by utilizing sample 5 as the seed. The resulting Fe_3O_4 nanoparticles (sample 8) grew to a larger size (26.2±7.6 nm) from the original 22.2±4.5 nm, as shown in Figure 3.15. The lattice fringes of an isolated particle of sample 8 were obtained by

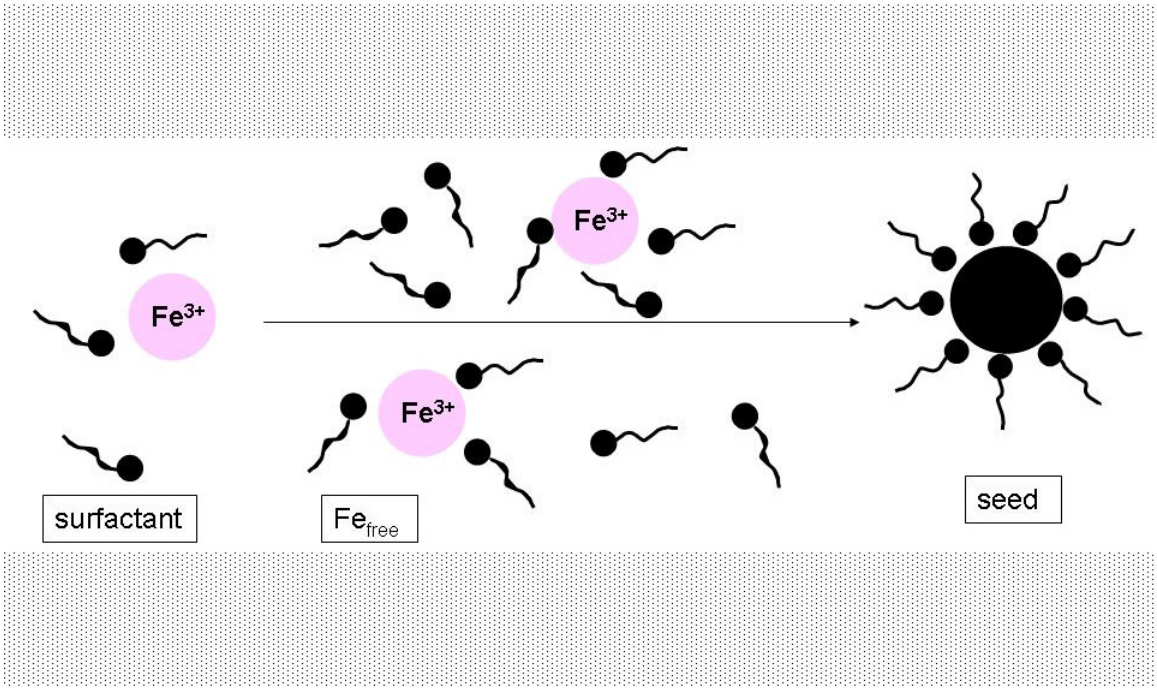

Figure 3.14: Effect of high S/Fe on Fe_3O_4 nanoparticle formation

high resolution TEM. The un-changed orientation of the lattice fringes throughout the entire particle indicates that the particle grew following the crystalline structure of the seed to become a single crystal nanoparticle (Figure 3.16). The smaller growth extent from 22.2 nm to 26.2 nm indicates that larger particles have a slower growth rate compared to smaller particles (compare to sample 5 which was seeded by 11 nm seeds) [103]. The particle size distribution of sample 5 (Figure 3.17a) was polydisperse because neither the nucleation nor the growth step was suppressed during Fe_3O_4 formation although seeds were monodisperse (Figure 3.7b). Sample 8 exhibited a similar behavior, i.e. the particle growth step did not dominate, leading to a bimodal particle distribution as shown in Figure 3.17b.

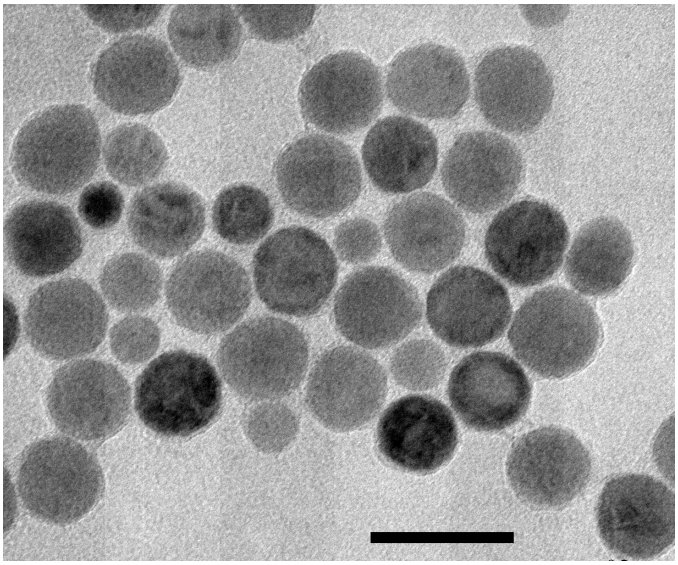

Figure 3.15: TEM image of Fe_3O_4 nanoparticles (sample 8) synthesized with the same conditions as sample 5, except using sample 5 as seeds. (scale bar = 50nm)

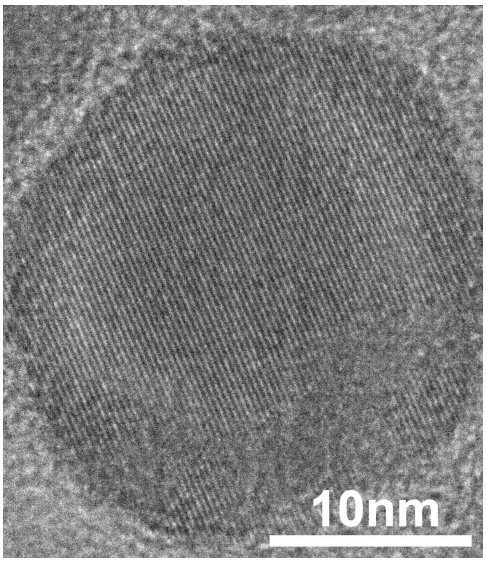

Figure 3.16: High resolution TEM image of a single Fe_3O_4 nanoparticle.

3.3.2.3 Magnetic properties of Fe_3O_4 nanoparticles

Figure 3.18 shows the room temperature magnetization as a function of applied magnetic field for samples 5 and 8. There is hysteresis present for sample 8 with a coercivity (H_c) of 50 Oe, which is consistent with ferrimagnetic behavior. The D_{avg} of 26.2±7.6 below the 50-60 nm critical limit (D_{SD})for Fe_3O_4 single magnetic domains suggests that sample 8 did not consist of magnetic multi-domains [98]. The weaker H_c (50 Oe) compared to 200 Oe obtained from the 70 nm Fe_3O_4 nanoparticles contributes to thermal effects in the single-domain region [97]. This means that the thermal energy provided from the nanoparticle surroundings significantly reduced the particle magnetization sustained by the anisotropy energy(KV), which is weaker for smaller particle sizes [41]. There is a small hysteresis (H_c=5 Oe) observed for sample 5 as shown in the insert of Figure 3.18. It has been reported in literature that the Fe_3O_4 critical size (D_{SP}) for superparamagnetic to ferrimagnetic transition lies between 25 nm and 30 nm [98]. As shown in Figure 3.17a, 40% and 10% of the number of nanoparticles in sample 5 are larger than 25 and 30 nm, respectively. Therefore, it could be concluded that the D_{SP} is near 30 nm, since the small observed coercivity (5 Oe) should arise from the lower amount of nanoparticles present. The D_{SP} of 30 nm is not generally accurate for pure Fe_3O_4 since the synthesized nanoparticles were non-stoichiometric Fe_3O_4. However, it provides valuable evidence for confirming the accurate D_{SP} of Fe_3O_4 which lies near 30 nm. It was also observed that the saturation magnetization (M_s) of samples 5 and 8 is lower than the bulk value of Fe_3O_4 (90 emu/g) due to spin disorder arising from

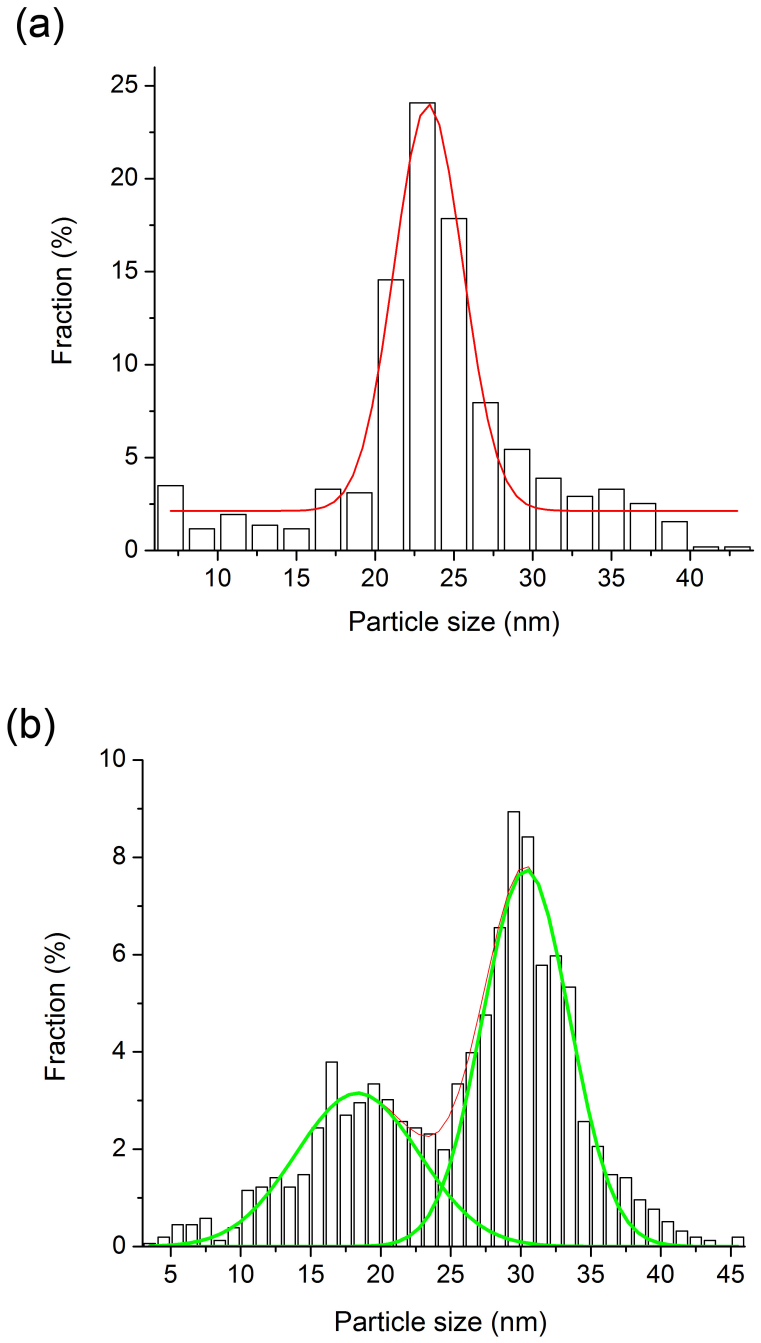

Figure 3.17: Particle distribution of: (a) sample 5 (seeds for sample 8); and (b) sample 8.

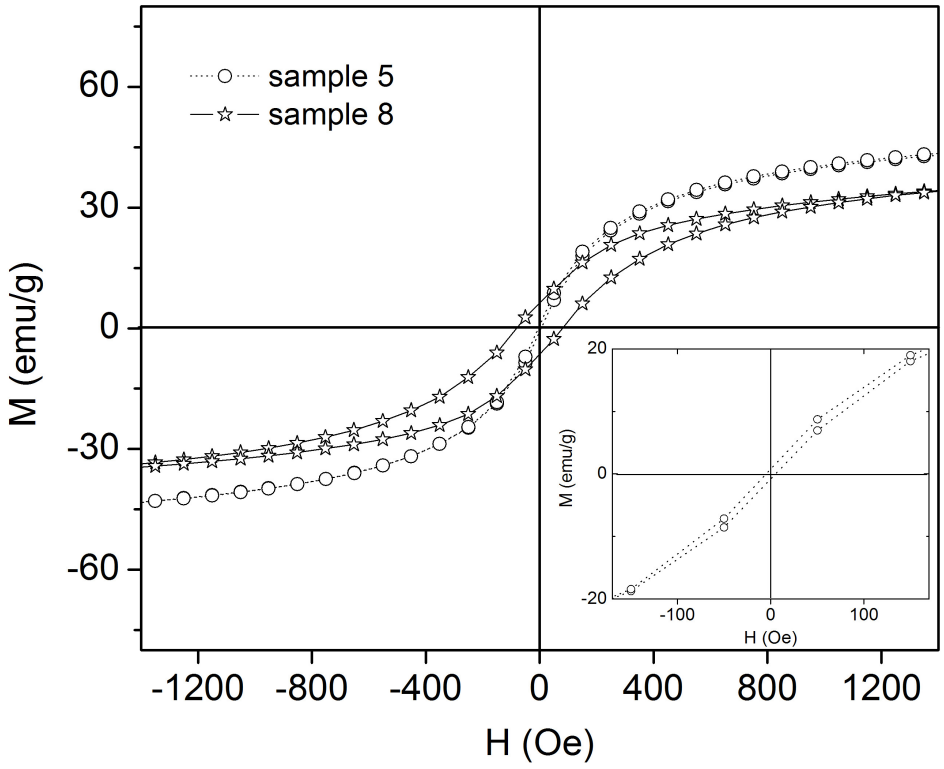

Figure 3.18: Magnetization (M) vs applied magnetic field (H) for samples 5 and 8 at 300 K.

the larger particle surface area (smaller particle) as suggested in literature [106].

3.3.2.4 Magneto-dielectric properties of the Fe_3O_4-polymer composites

The measured relative dielectric permittivity (ε_r) and magnetic permeability (μ_r) values of the polymer composites with surfactant modified Fe_3O_4 nanoparticles are shown in Figure 3.19. The ε_r of the polymer composite (SEBS) (ε_r=2.4) improved from 2.4 to 3.0 with increasing amount of Fe_3O_4 nanoparticle doping. The dielectric loss (tanδ) was kept below 0.015 as shown in Figure 3.20. Sample 8

and the nanoparticle sample used to seed the growth of larger particle sizes, which have the highest size difference (from 11.1 to 26.2 nm), show the same value of ε_r. This indicates that particle size does not affect the dielectric permittivity (ε_r) of the polymer composites. However, the μ_r of the SEBS polymer composite (μ_r= 1) did not always increase with addition of Fe_3O_4 nanoparticles. The composite with 8 wt% of 11 nm Fe_3O_4 (seed) showed the same μ_r of 1 as the pure SEBS polymer. This suggests that the thermal energy provided by the particle surroundings significantly lowers the magnetization of the polymer composite since the 11 nm Fe_3O_4 nanoparticles are superparamagnetic. For composites with single-domain Fe_3O_4 nanoparticles (samples 5 and 8), the higher μ_r values were obtained with smaller amounts of larger size particles (sample 8). This is because larger particles result in higher anisotropy energies (KV), which is needed to overcome the demagnetization arising from thermal energy effects. Therefore, a larger particle size is one of the major contributing factors required to maintain the particle's magnetization and to obtain higher values of μ_r when the particle size is within the magnetic single-domain region.

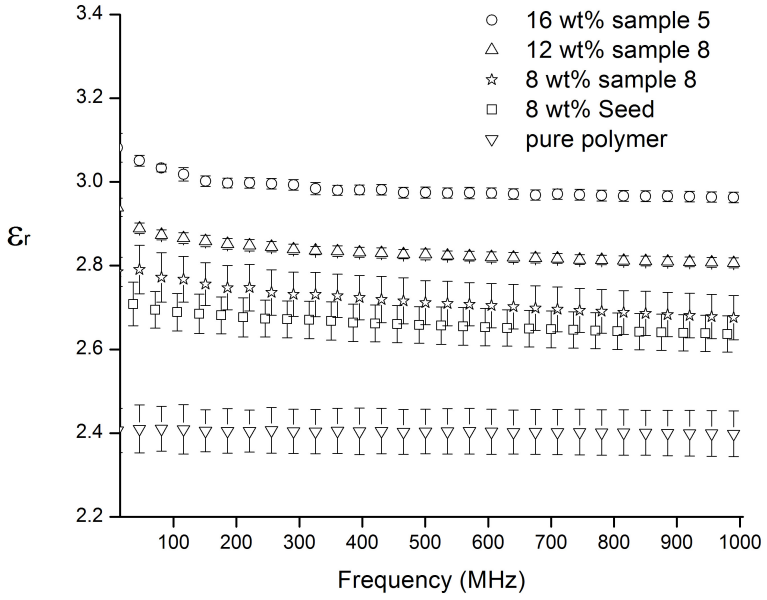

(a) ε_r

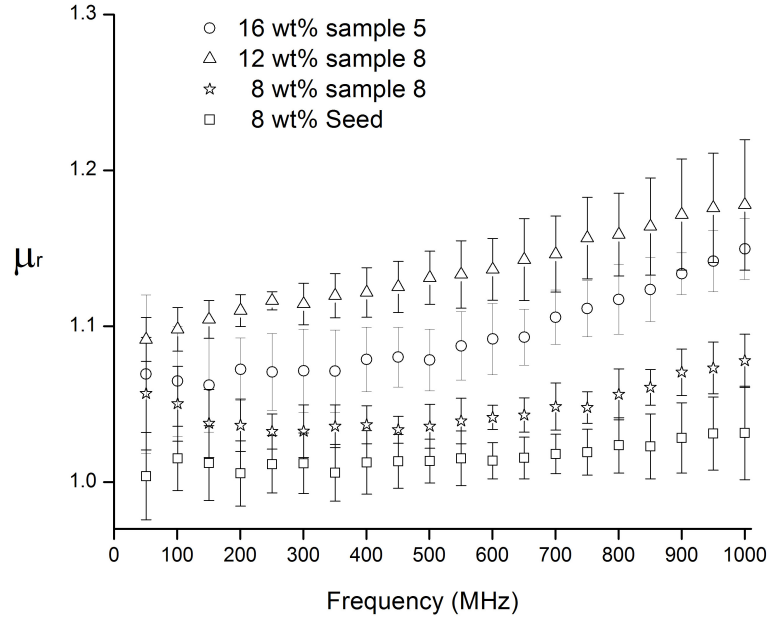

(b) μ_r

Figure 3.19: High frequency relative permittivity (ε_r) and magnetic permeability (μ_r) of surfactant-modified Fe_3O_4 nanocomposites at room temperature.

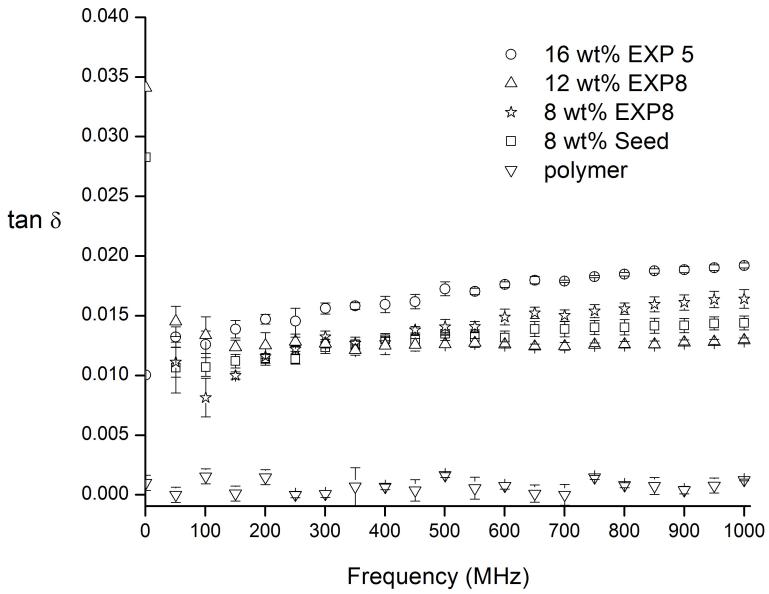

Figure 3.20: Dielectric loss (tanδ) of surfactant-modified Fe_3O_4 nanocomposites at high frequency range.

3.3.2.5 Conclusions

We have demonstrated the feasibility of a seed-mediated method to synthesize surfactant-modified Fe_3O_4 nanoparticles with various particle distributions. The surfactant and Fe-precursor play a crucial role in determining the particle nucleation and growth rate and lead to different nanoparticle sizes. In addition, the size of the seeds also led to different Fe_3O_4 growth extent and particle distributions because both nucleation and growth steps occurred during synthesis. The dielectric permittivity (ε_r) of the polymer nanoparticle composite increased by adding surfactant modified-Fe_3O_4 nanoparticles, and particle size did not significantly influence ε_r. However, higher magnetic permeabilities (μ_r) were obtained using larger Fe_3O_4 nanoparticles. This is because a higher anisotropy energy (KV) can overcome

thermal effects from the particle surroundings and sustain a high magnetization.

3.3.3 Magneto-dielectric Properties of Surface-modified Nickel Zinc Ferrite Nanocomposites

The seed-mediated growth method was also utilized to synthesize surface-modified nickel zinc ferrite ($Ni_xZn_{1-x}Fe_2O_4$) nanoparticles with various sizes and shapes. These ferrites have intrinsically higher permeability and less loss compared to Fe_3O_4.

3.3.3.1 Surface-modified nickel zinc ferrite nanoparticles

The seeds used to grow larger surfactant-modified nickel zinc iron oxide nanoparticles were non-spherical with shape anisotropy, as shown in Figure 3.21 [107]. The average size (D_{avg}) measured from TEM was 13.2±3.8 nm. Figure 3.22 depicts a selected area electron diffraction pattern from the synthesized nanoparticles in Figure 3.21 and shows multiple diffraction rings. As shown in Table 3.4, the calculated lattice d-spacings derived from the diffraction rings fall between those of $NiFe_2O_4$ and $ZnFe_2O_4$ reported in literature, indicating that the nickel zinc ferrite nanoparticles were synthesized ($Ni_xZn_{1-x}Fe_2O_4$) [108].

Figure 3.23 confirmed that larger $Ni_xZn_{1-x}Fe_2O_4$ nanoparticles (17.3±5.6 nm) can also be synthesized using 13.2±3.8 nm nanoparticles as growth seeds. However, Figure 3.24 shows that smaller nanoparticles with broader particle size distribution (16.1±9.2 nm) were synthesized with the same conditions as 17.3±5.6 nm nanoparticles, except using 17.3±5.6 nm nanoparticles as the seeds (see Section 3.2 for detailed synthesis conditions). These results indicate that it is necessary

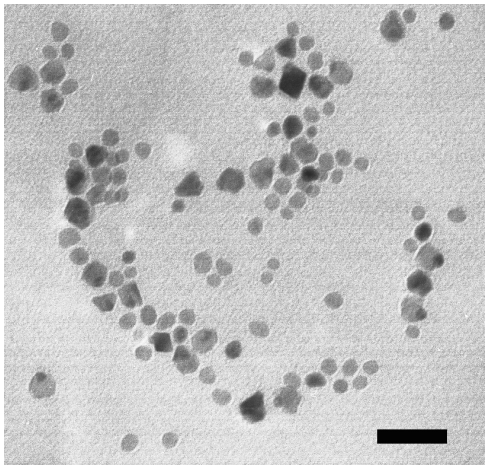

(a) TEM image.

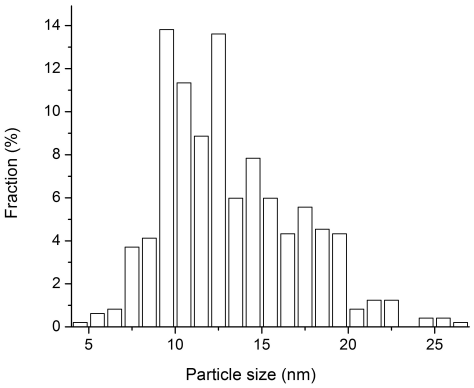

(b) Particle size distribution.

Figure 3.21: TEM image of $Ni_xZn_{1-x}Fe_2O_4$ nanoparticles (scale bar = 50nm).

d	2.978	2.512	2.100	1.488
hkl	220	311	400	440
$ZnFe_2O_4$	2.986	2.546	2.111	1.493
$NiFe_2O_4$	2.947	2.513	2.084	1.473

Table 3.4: Lattice spacing of synthesized nanoparticles, d(Å), derived from the diffraction pattern shown in Figure 3.22. and standard lattice spacing for nickel ferrite ($NiFe_2O_4$) and zinc ferrite ($ZnFe_2O_4$) [108].

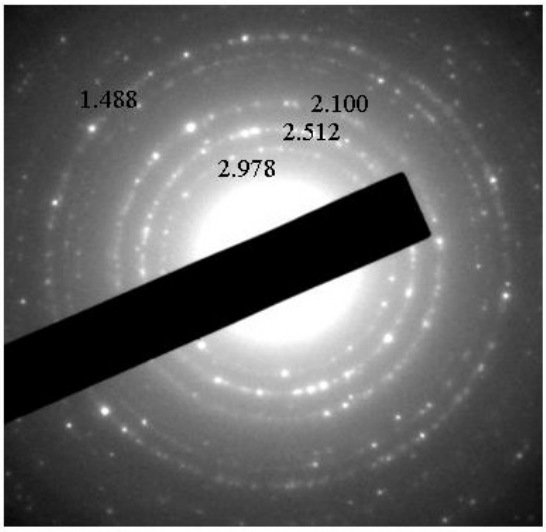

Figure 3.22: Selected area electron diffraction pattern of $Ni_xZn_{1-x}Fe_2O_4$ nanoparticles.

to utilize nanoparticles with a narrow size distribution as the seeds for growing larger particles.

3.3.3.2 Magneto-dielectric properties of the $Ni_xZn_{1-x}Fe_2O_4$ / polymer composites

The relative dielectric permittivity and magnetic permeability of the polymer nanocomposites with surfactant-modified 17.3±5.6 nm nickel zinc iron oxide ($Ni_xZn_{1-x}Fe_2O_4$) nanoparticles are shown in Figures 3.25a and 3.25b, respectively. The relative permittivity of the SEBS copolymer ($\varepsilon_r = 2.4$) improved from 2.4 to 2.9 with increasing amount of $Ni_xZn_{1-x}Fe_2O_4$ nanoparticles. The dielectric loss (tanδ) was kept below 0.01 as shown in Figure 3.26. The magnetic permeability of the SEBS copolymer (μ_r= 1) also improved from 1.0 to 1.5 at 1 GHz with increasing

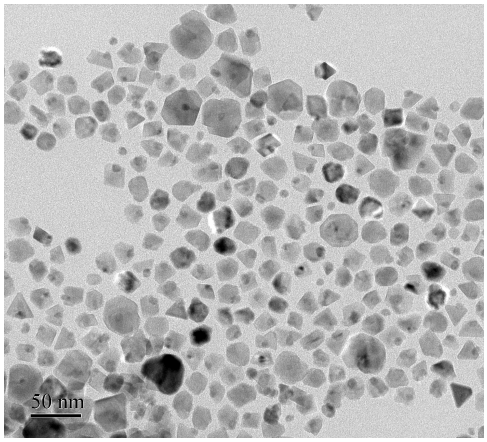

(a) TEM image.

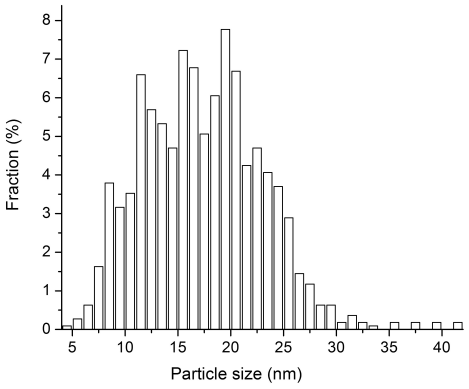

(b) Particle size distribution.

Figure 3.23: TEM image of $Ni_xZn_{1-x}Fe_2O_4$ nanoparticles synthesized by the seed-mediated method.

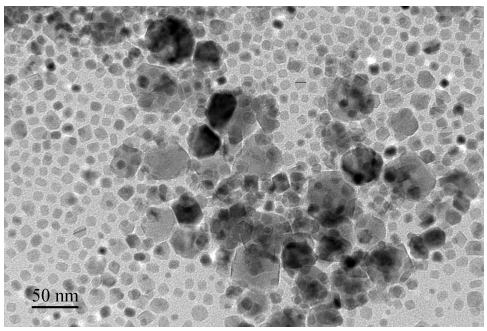

(a) TEM image.

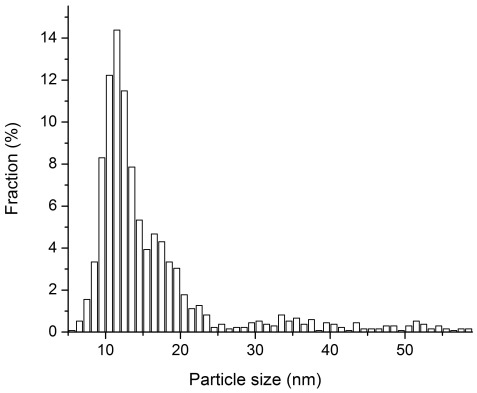

(b) Particle size distribution.

Figure 3.24: TEM image of $Ni_xZn_{1-x}Fe_2O_4$ nanoparticles synthesized by the seed-mediated method.

amounts of $Ni_xZn_{1-x}Fe_2O_4$ nanoparticle doping.

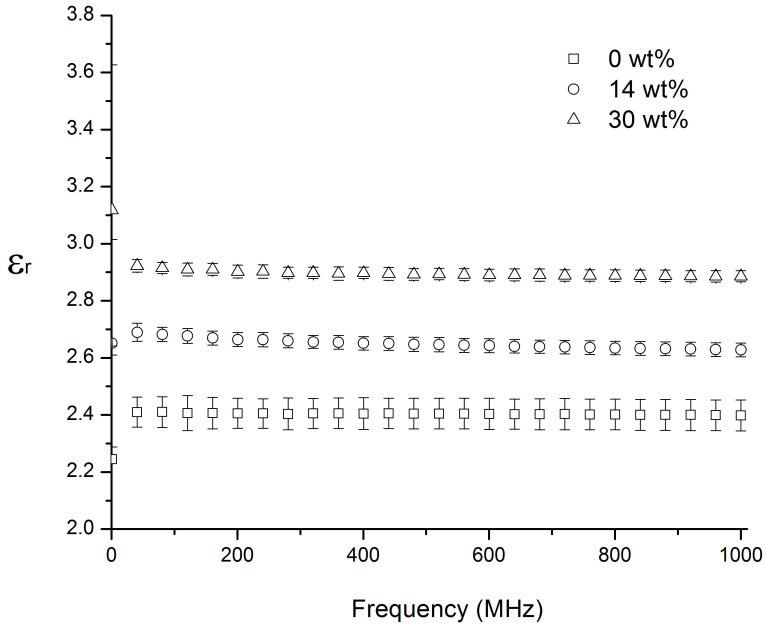

(a) Relative dielectric permittivity

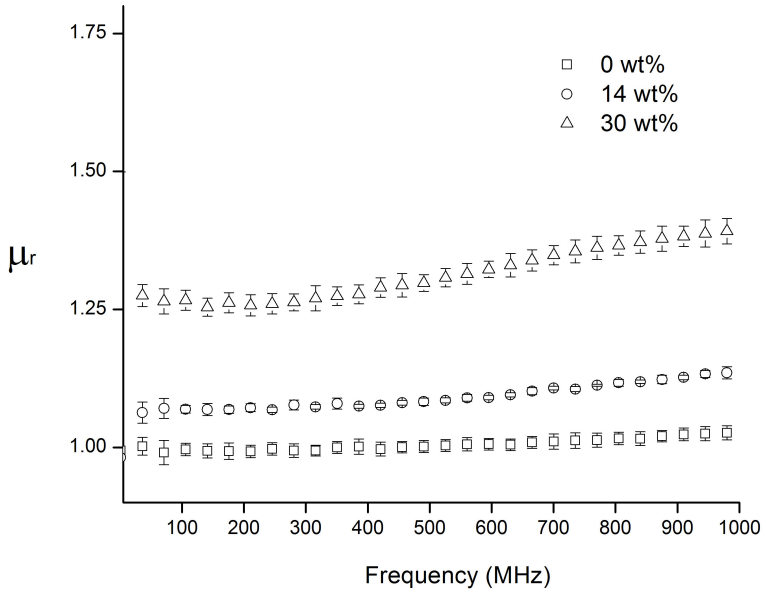

(b) Relative magnetic permeability

Figure 3.25: Relative permittivity and magnetic permeability of surfactant-modified $Ni_xZn_{1-x}Fe_2O_4$ composites.

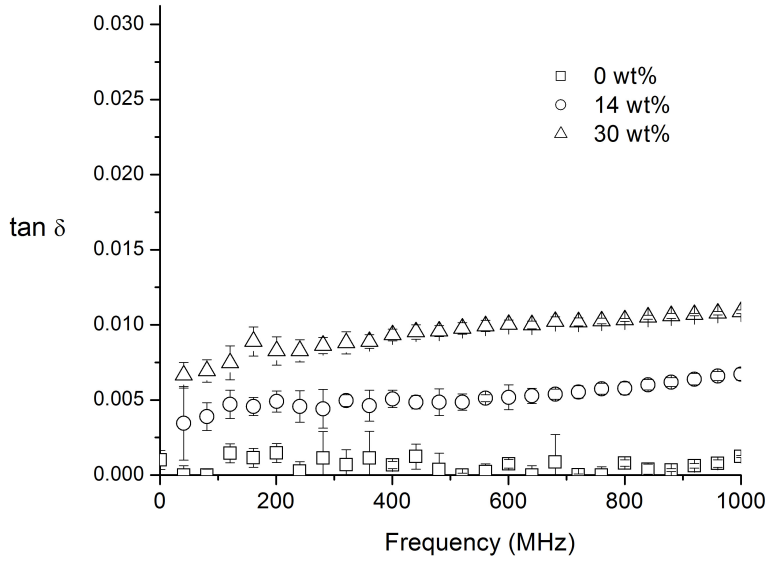

Figure 3.26: Dielectric loss (tanδ) of surfactant-modified $Ni_xZn_{1-x}Fe_2O_4$ nanocomposites at high frequency range.

3.3.3.3 Conclusions

Surfactant-modified $Ni_xZn_{1-x}Fe_2O_4$ nanoparticles with various particle distributions were successfully synthesized using a seed-mediated method. Growth seeds with broad particle size distribution have an adverse affect on the particle growth from nuclei although seeds with narrow size distribution present in solution promote $Ni_xZn_{1-x}Fe_2O_4$ formation in favor of particle growth. The dielectric permittivity (ε_r) and magnetic permeability (μ_r) of the polymer nanoparticle composites increased by adding surfactant-modified $Ni_xZn_{1-x}Fe_2O_4$ nanoparticles. The polymer composite with 30 wt% of modified $Ni_xZn_{1-x}Fe_2O_4$ nanoparticles produced values of μ_r and ε_r of 1.5 and 2.9 respectively, with dielectric tanδ less than 0.01 within a 1 GHz frequency range.

Chapter 4

Conclusions and Future Work

We have demonstrated the feasibility of producing high dielectric permittivity nanoparticles (TiO_2) uniformly dispersed within polymer matrices. All nanoparticles were confined within the crosslinked sulfonated styrene blocks and no effect was observed on the phase separation behavior of the S-SEBS block copolymer. Dielectric experiments showed that higher permittivity composites can thus be obtained with a significant decrease in loss ($\tan\delta$ <0.01) when crosslinked with vinyltrimethoxysilane. Therefore, there are many opportunities to manipulate the magneto-dielectric properties of the composites by incorporating magneto-dielectric nanoparticles within block copolymer matrices. The block copolymer phase separated microstructures with strong cation associating functional groups could be utilized to nucleate, grow, and template different size, shape, and ordering of the magneto-dielectric particles with various chemical compositions.

Furthermore, various surface-modified magneto-dielectric particles differing in shape and size were successfully synthesized with improved compatibility with glassy styrene/rubbery block copolymers. The desired properties of the composites are

high relative permeability (μ_r) and high ratio of relative permeability to permittivity (μ_r/ε_r), which are the critical factors for microwave communication devices. The experimental results showed that the nanocomposites' magnetic permeabilities significantly depend on the characteristic length (size and shape) of the doped magneto-dielectric particles although they are flexible and easily to process. The optimum size range for magneto-dielectric particles to obtain high magnetic permeability is between 30 and 100 nm, where single domain ferromagnetic particles without any domain wall are present. For the particles with magnetic multi-domains (size larger than approximate 100 nm), the polymer composite's magnetic permeability is low at the GHz frequency range due to particle magnetic domain wall movement. When magnetic particles are subject to a magnetic field, the boundaries of the particles' magnetic domain walls move to align with the direction of applied field. More domain wall movement results in less ability to respond to the applied magnetic alternating field (GHz), thus leading to lower magnetization and magnetic permeability. Magnetic nanoparticles become superparmagnetic when the particle size is below 30 nm approximately. At the superparamagnetic state, the anisotropy energy sustaining the particle's magnetization becomes comparable to the thermal energy from the magnetic nanoparticle surroundings. Therefore, thermal energy effects cause significant fluctuations in nanoparticles' magnetic moments and reduces their resultant magnetic magnetization and magnetic permeability.

The best strategy to obtain high magnetic permeability, is to tailor the nanoparticle size between 30 and 100 nm to avoid the adverse effects of thermal energy fluctuations and associated domain wall movement. Thermal energy fluctuation effects

can be overcome by increasing the anisotropy energy of the magnetic particles. This means that irregular shaped instead of spherical nanoparticles with particle size near 30 nm are desirable. In terms of low energy loss, the nanoparticles doped within the polymer matrix should exhibit low electrical conductivity. Materials with high electrical conductivity tend to dissipate the electrons stored or induced during electromagnetic wave transmission and therefore cause energy loss. Ferromagnetic metals or alloys, such as cobalt (Co), iron (Fe), iron-platinum ($Fe-Pt$), and samarium-cobalt ($Sm-Co$), are not suitable as nanoparticle dopants to increase the magnetic permeability of the nanocomposite due to their high electrical conductivity and thus high loss. Nickel zinc ferrites $Ni_xZn_{1-x}Fe_2O_4$ are promising magnetic materials for high permeability nanocomposites since they can be easily magnetized (they are soft ferrites) and display low electrical conductivity. In addition, magneto-dielectric nanoparticles with single magnetic domains and shape anisotropy have been confirmed to be the critical factors for optimum magneto-dielectric properties in RF nanocomposites, as shown in Section 3.3.1. It is feasible to grow such nanoparticles with anisotropic shape utilizing block copolymer templates and the seed-mediated growth method shown in Chapter 2 and Chapter 3, respectively. The adverse effect of growth seeds with broad particle size distribution could be overcome by a size-selective precipitation method, which involves sorting the particle size using a solvent/non-solvent pair [109, 110]. By adding a non-solvent into a particle solution to approach its partial flocculation, bigger particles will aggregate first because they experience stronger attractive forces compared to smaller particles. Thus, centrifuging the solution will separate the bigger particles from smaller particles, leading to

a particle solution with narrower particle size distribution. Ferrites with different particle chemical compositions, $Ni_xZn_{1-x}Fe_2O_4$ as an example, exhibit improved magneto-dielectric properties [111]. Thus, tailoring the ferrite's chemical compositions can result in composites with improved (μ_r), (ε_r), and lower tan δ. Moveover, it is also important to evaluate the effect of particle orientation within polymer matrices on the magneto-dielectric properties of the resultant composite. A particular orientation of particles within polymer matrices could be accomplished by utilizing block copolymer self-assembled microstructures. Alternatively, a layer-by-layer technique is also feasible for preparing polymer composites with layered nanoparticles. This technique involves alternatively stacking thin polymer films with and without doped magnetic nanoparticles and applying temperature and pressure to form bulk polymer composites containing layered magnetic nanoparticles. The spacing between two layers can be easily controlled by changing polymer film thickness, resulting in polymer composites with desired numbers of layers.

Bibliography

[1] Chui, S. T., Hu, L.; "Theoretical investigation on the possibility of preparing left-handed materials in metallic magnetic granular composites" *Physical Review B* 2002, 65, 144407.

[2] Mosallaei, H., Sarabandi, K.; "Magneto-dielectrics in electromagnetics: concept and applications" *IEEE Transactions on Antennas and Propagation* 2004, 52(6), 1558.

[3] Bockstaller, M. R., Mickiewicz, R. A., Thomas, E. L.; "Block copolymer nanocomposites: perspectives for tailored functional materials" *Advanced Materials* 2005, 17 (11), 1331.

[4] Ozbay, E., Aydin, K., Cubukcu, E., Bayindir, M.; "Transmission and reflection properties of composite double negative metamaterials in free space" *IEEE Transactions on Antennas and Propagation* 2003, 51(10), 2592.

[5] Vanderah, T. A.; "Talking ceramics" *Science* 2002, 298, 1182.

[6] Siegrist, T., Vanderah, T. A.; "Combining magnets and dielectrics: crystal chemistry in the BaO-Fe2O3-TiO2 system" *European Journal of Inorganic Chemistry* 2003, 2003(8), 1483.

[7] Naito, Y., Suetake, K.; "Application of ferrite to electromagnetic wave absorber and its characteristics" *IEEE Transactions on Microwave Theory and Techniques* 1971, MT19(1), 65.

[8] Kim, S. S., Jo, S. B., Gueon, K. I., Choi, K. K., Kim, J. M., Chum, K. S.; "Complex permeability and permittivity and microwave absorption of ferrite-rubber composite in X-band frequencies" *IEEE Transactions on Magnetics* 1991, 27(6), 5462.

[9] Kazantseva, N. E., Ryvkina, N. G., Chmutin, I. A.; "Promising materials for microwave absorbers " *Journal of Communications Technology and Electronics* 2003, 48(2), 173.

[10] Buerkle, A. and Sarabandi, K.; "A wide-Band, circularly polarized, magnetodielectric resonator antenna" *IEEE Transactions on Antennas and Propagation* 2005, 53(11), 3436.

[11] Kim, D. Y., Chung, Y. C., Kang, T. W., Kim, H. C.; "Dependence of microwave absorbing property on ferrite volume fraction in MnZn ferrite-rubber composites" *IEEE Transactions on Magnetics* 1996, 32(2), 555.

[12] Singh, P., Babbar, V. K., Razdan, A., Puri, R. K., Goel, T. C.; "Complex permittivity, permeability, and X-band microwave absorption of CaCoTi ferrite composites " *Journal of Applied Physics* 2000, 87(9), 4362.

[13] Anantharaman, M. R., Malini, K. A., Sindhu, S., Mohammed, E. M., Date, S. K., Kulkarni, S. D., Joy, P. A., Kurian. P.; "Tailoring magnetic and dielectric properties of rubber ferrite composites containing mixed ferrites" *Bulletin of Materials Science* 2001, 24(6), 623.

[14] Peng, C. H., Wang, H. W., Kan, S. W., Shen, M. Z., Wei, Y. M., Chen, S. Y.; "Microwave absorbing materials using Ag-NiZn ferrite core-shell nanopowders as fillers " *Journal of Magnetism and Magnetic Materials* 2004, 284, 113.

[15] Chen, Y. J., Cao, M. S., Wang, T. H., Wan, Q.; "Microwave absorption properties of the ZnO nanowire-polyester composites" *Applied Physics Letters* 2004, 84(17), 3367.

[16] Lim, K. M., Lee, K. A., Kim, M. C., Park, C. G.; "Complex permeability and electromagnetic wave absorption properties of amorphous alloy-epoxy composites " *Journal of Non-crystalline Solids* 2005, 351, 75.

[17] Sindhu, S., Jegadesan, S., Parthiban, A., Valiyaveettil, S.; "Synthesis and characterization of ferrite nanocomposite spheres from hydroxylated polymers" *Journal of Magnetism and Magnetic Materials* 2006, 296, 104.

[18] Nan, C. W.; "Physics of inhomogeneous inorganic materisls" *Progress in Materials Science* 1993, 37, 1.

[19] Neelakanta, P. S.; *Handbook of Electromagnetic Materials: Monolithic and Composite Versions and Their Applications* 1995, CRC Press, Boca Raton, p133.

[20] Tuncer, E., Serdyuk, Y. V., Gubanski, S. M.; "Dielectric mixtures: Electrical properties and Modeling" *IEEE Transactions on Dielectrics and Electrical Insulation* 2002, 9(5), 809.

[21] Kittel, C.; "Theory of the structure of ferromagnetic domains in films and small particles" *Physical Review* 1946, 70, 965.

[22] Kodama, R. H.; "Magnetic nanoparticles" *Journal of Magnetism and Magnetic Materials* 1999, 200, 359.

[23] Batlle, X., Labarta, A.; "Finite-size effects in fine particles: magnetic and transport properties" *Journal of Physics D: Applied Physics* 2002, 35(6), R15.

[24] Willard, M. A., Kurihara, L. K., Carpenter, E. E., Calvin, S., Harris, V. G. ; "Chemically prepared magnetic nanoparticles" *International Materials Reviews* 2004, 49(3-4), 125.

[25] Forster, S., Antonietti, M.; "Amphiphilic block copolymers in structure-controlled nanomaterial hybrids" *Advanced Materials* 1998, 10(3), 195.

[26] Park, C., Yoon, J., Thomas, E. L.; "Enabling nanotechnology with self assembled block copolymer patterns" *Polymer* 2003, 44, 6725.

[27] Cushing, B. L., Kolesnichenko, V. L., O'Connor, C. J.; "Recent advances in the liquid-phase syntheses of inorganic nanoparticles" *Chemical Reviews* 2004, 104(9), 3893.

[28] Farrell, D., Majetich, S. A., Wilcoxon, J. P.; "Preparation and characterization of monodisperse Fe nanoparticles " *The Journal of Physical Chemistry B* 2003, 107(40), 11022.

[29] Park, J., An, K. J., Hwang, Y. S., Park, J. G., Noh, H. J., Kim, J. Y., Park, J. H., Hwang, N. M., Hyeon, T.; "Ultra-large-scale syntheses of monodisperse nanocrystals " *Nature Materials* 2004, 3(12), 891.

[30] Farrell, D., Cheng, Y., McCallum, R. W., Sachan, M., Majetich, S. A.; "Magnetic interactions of iron nanoparticles in arrays and dilute dispersions" *The Journal of Physical Chemistry B* 2005, 109(28), 13409.

[31] Zhao, S. Y., Lee, D. K., Kim, C. W., Cha, R. G., Kim, Y. H., Kang, Y. S.; "Synthesis of magnetic nanoparticles of Fe_3O_4 and $CoFe_2O_4$ and their surface modification by surfactant adsorption " *Bulletin of the Korean Chemical Society* 2006, 27(2), 237.

[32] Ku, C. C., Liepins, R.; *Electrical Properties of Polymers: Chemical Principles* 1987, Macmillan publishing company, New York.

[33] Blythe, A. R., Bloor, D. *Electrical Properties of Polymers* 2005, Cambridge University Press, New York. p33.

[34] Pohl, H. A.; "Superdielectrics polymers" *IEEE Transactions on Electrical Insulation* 1986, 21(5), 683.

[35] Allen, G., Bevington, J. C.; *Comprehensive Polymer Science : the Synthesis, Characterization, Reactions & Applications of Polymers* 1989, Pergamon Press, New York, Vol 2, Ch18.

[36] Maxwell Garnett, J. C.; "Colours in metal glasses and in metallic films" *Philosophical Transactions of the Royal Society of London. Series A* 1904 , 203, 385.

[37] Goncharenko, A. V.; "Generalizations of the Bruggeman equation and a concept of shape-distributed particle composites" *Physical Review E.* 2003, 68, 041108.

[38] Myroshnychenko, V., Brosseau, C.; "Finite-element method for calculation of the effective permittivity of random inhomogeneous media" *Physical Review E.* 2005, 71, 016701.

[39] Chiang, Y. M., Birnie, D. P., Kingery, W. D.; *Physical Ceramics : Principles for Ceramic Science and Engineering* 1997, John Wiley & Sons, Inc., New York.

[40] Skomski, R.; "Nanomagnetics" *Journal of Physics: Condensed Matter* 2003, 15(20), R841.

[41] Spaldin, N. A.; *Magnetic Materials : Fundamentals and Device Applications* 2003, Cambridge University Press, New York.

[42] LesliePelecky, D. L., Rieke, R. D.; "Magnetic properties of nanostructured materials" *Chemistry of Materials* 1996, 8, 1770.

[43] Moulson, A. J., Herbert, J. M.; *Electroceramics : materials, properties, applications* 2003, 2nd ed, West Sussex, New York, Wiley.

[44] Valenzuela, R. *Magnetic Ceramics* Cambridge ; New York : Cambridge University Press, 1994.

[45] Bodker, F., Morup, S.; "Size dependence of the properties of hematite nanoparticles" *Europhysics Letters* 2000, 52, 217.

[46] Bodker, F., Morup, S., Linderoth, S.; "Surface effects in metallic iron nanoparticles" *Physical Review Letters* 1994, 72, 282.

[47] Shamonin, M., Snarskii, A., Zhenirovskyy, M. "Effective magnetic permeability of ferromagnetic composites. Theoretical description and comparison with experiment" *NDT & E International* 2004, 37 (1), 35.

[48] Waki, H., Igarashi, H., Honma, T.; "Estimation of ettective permeability of magnetic composite materials " *IEEE Transactions on Magnetics* 2005, 41(5), 1520.

[49] Rozanov, K. N., Li, Z. W., Chen, L. F., Koledintseva, M. Y.; "Microwave permeability of Co_2Z composites" *Journal of Applied Physics* 2005, 97, 013905.

[50] Brosseau, C., Talbot, P.; "Effective magnetic permeability of Ni and Co micro- and nanoparticles embedded in a ZnO matrix" *Journal of Applied Physics* 2005, 97, 104325.

[51] Hamley, Ian W.; *Developments in block copolymer science and technology* c2004 Chichester, West Sussex, England ; Hoboken, NJ : J. Wiley.

[52] Bates, F. S., Fredrickson, G. H.; " Block copolymer thermodynamics - theory and eperiment" *Annual Review of Physical Chemistry* 1990, 41, 525.

[53] Bates, F. S.; "Polymer-Polymer phase behavior" *Science* 1991, 251, 898.

[54] Khandpur, A. K., Foerster, S., Bates, F. S., Hamley, I. W., Ryan, A. J., Bras, W., Almdal, K., Mortensen, K.; "Polyisoprene-Polystyrene diblock copolymer phase diagram near the order-disorder transition" *Macromolecules* 1995, 28, 8796.

[55] Matsen, M. W., Thompson, R. B.; "Equilibrium behavior of symmetric ABA triblock copolymer melts" *Journal of Chemical Physics* 1999, 111, 7139.

[56] Honeker, C. C., Thomas, E. L.; "Impact of morphological orientation in determining mechanical properties in triblock copolymer systems " *Chemistry of Materials* 1996, 8(8), 1702.

[57] Bumjoon, Kim J., Bang, Joona, Hawker, Craig J., Kramer, Edward J. ; "Effect of areal chain density on the location of polymer-modified gold nanoparticles in a block copolymer template" *Macromolecules* 2006, 39 (12), 4108.

[58] Kang, H., Detcheverry, F. A., Mangham, A. N., Stoykovich, M. P., Daoulas, K. C., Hamers, R. J., Muller, M., Pablo, J. J., Nealey, P. F.; "Hierarchical assembly of nanoparticle superstructures from block copolymer-nanoparticle composites" *Physical Review Letters* 2008, 100, 148303.

[59] Bockstaller, M. R., Lapetnikov, Y., Margel, S., Thomas, E. L.; "Size-Selective organization of enthalpic compatibilized nanocrystals in ternary block copolymer/particle Mixtures" *Journal of the American Chemical Society* 2003, 125(18), 5276.

[60] Lin, Y., Boker, A., He, J. B., Sill, K, Xiang, H. Q., Abetz, C., Li, X. F., Wang, J., Emrick, T., Long, S., Wang, Q., Balazs, A., Russell, T. P.; "Self-directed self-assembly of nanoparticle/copolymer mixtures " *Nature* 2005, 434, 55.

[61] Chou, K. S., Huang, K. C.; "Studies on the chemical synthesis of nanosized nickel powder and its stability" *Journal of Nanoparticle Research* 2001, 3, 127.

[62] Huang, K. C., Ehrman, S. H.; "Synthesis of iron nanoparticles via chemical reduction with palladium ion seeds "*Langmuir* 2007, 23, 1419.

[63] Ge, J. P., Hu, Y. X., Biasini, M., Dong, C. L., Guo, J. H., Beyermann, W. P., Yin, Y. D.; "One-step synthesis of highly water-soluble magnetite colloidal nanocrystals" *Chemistry : A European Journal* 2007, 13(25), 7153.

[64] Sun, S., Zeng, H., Robinson, D. B., Raoux, S., Rice, P. M., Wang, S. X., Li, G.; "Monodisperse MFe2O4 (M=Fe, Co, Mn) nanoparticles" *Journal of the American Chemcial Society* 2004, 126, 273.

[65] Yin, M., Willis, A., Redl, F., Turro, N. J., O'Brien, S. P.; "Influence of capping groups on the synthesis of gamma-Fe2O3 nanocrystals" *Journal of Materials Research* 2004, 19, 1208.

[66] Zhang, Q. M.; Li, H.; Poh, M.; Xu, H.; Cheng, Z.-Y.; Xia, F.; Huang, C.; "An all-organic composite actuator material with a high dielectric constant" *Nature* 2002, 419, 284.

[67] Choa, S. D., Lee, J. Y., Hyuna, J. G., Paik, K. W.; "Study on epoxy/$BaTiO_3$ composite embedded capacitor films (ECFs) for organic substrate applications "*Materials Science and Engineering: B* 2004, 110, 233.

[68] Pothukuchi, S., Li, Y., Wong, C. P.; "Development of a novel polymer-metal nanocomposite obtained through the route of in situ reduction for integral capacitor application" *Journal of Applied Polymer Science* 2004, 93, 1531.

[69] Dang, Z. M.; Fan, L. Z.; Shen, Y.; Nan, C. W.; "Study on dielectric behavior of a three-phase CF/(PVDF+$BaTiO_3$) composite" *Chemical Physics Letters* 2003, 369(1-2), 95.

[70] Dang, Z. M., Fan, L. Z., Shen, Y., Nan, C. W.; "Dielectric behavior of novel three-phase MWNTs/$BaTiO_3$/PVDF composites" *Materials Science and Engineering: B* 2003, 103(2), 140.

[71] Bai, Y., Cheng, Z. Y., Bharti, V., Xu, H., Zhang, Q. M.; "High-dielectric-constant ceramic-powder polymer composites" *Applied Physics Letters* 2000, 76, 3804.

[72] Wang, J. W., Shen, Q. D., Yang, C. Z., Zhang, Q. M.; "High dielectric constant composite of P(VDF-TrFE) with grafted copper phthalocyanine oligomer " *Macromolecules* 2004, 37(6), 2294.

[73] Fiske, T. J., Gokturk, H. S., Kalyon, D. M. ; "Percolation in magnetic composites " *Journal of Materials Science* 1997, 32(20), 5551.

[74] Kalyon, D. M., Birinci, E., Yazici, R., Karuv, B., Walsh, S.; "Electrical properties of composites as affected by the degree of mixedness of the conductive filler in the polymer matrix " *Polymer Engineering and Science* 2002, 42(7), 1609.

[75] Bogle, A., Kempel, L., Rothwell, E., Nyquist, D., Hawley, M., Schneider, S., Havrilla, M.; "Measurement techniques for ferromagnetic materials using a stripline" *IEEE AP-S International Symposium and URSI Radio Science Meeting* Columbus, Ohio, June 2003, 23.

[76] Heiser, J. A., King, J. A., Konell, J. P., Sutter, L. L.; "Electrical conductivity of carbon filled nylon 6,6" *Advances in Polymer Technology* 2004, 23(2), 135.

[77] Lim, K. M., Lee, K. A., Kim, M. C., Park, C. G.; "Complex permeability and electromagnetic wave absorption properties of amorphous alloyVepoxy composites " *Journal of Non-Crystalline Solids* 2005, 351(1), 75.

[78] Yashchyshyn, Y., Modelski, J. W.; "Rigorous analysis and investigations of the scan antennas on a ferroelectric substrate " *IEEE Transactions on Microwave Theory and Techniques* 2005, 53(2), 427.

[79] McCurrie, R. A.; *Ferromagnetic Materials: Structure and Properties* 1994, Academic Press, San Diego, CH 4.

[80] Pardavi-Horvath, M. ; "Microwave applications of soft ferrites" *Journal of Magnetism and Magnetic Materials* 2000, 215, 171.

[81] Du Trémolet de Lacheisserie, E., Gignoux, D., Schlenker, M.; *Magnetism II-Materials & Applications* 2002, Kluwer Academic Publishers, Norwell, Mass., Ch17.

[82] Yavuz, Ö., Ram, M. K., Aldissi, M., Poddar, P., Hariharan, S.; "Synthesis and the physical properties of MnZn ferrite and NiMnZn ferrite-polyaniline nanocomposite particles" *Journal of Materials Chemistry* 2005, 15, 810.

[83] Poddar, P., Wilson, J. L., Srikanth, H., Morrison, S. A., Carpenter, E. E.; "Magnetic properties of conducting polymer doped with manganese-zinc ferrite nanoparticles" *Nanotechnology* 2004, 15, S570.

[84] Wagner CD. *The NIST X-ray Photoelectron Spectroscopy (XPS) Database.* Gaithersburg, MD: U.S. Dept. of Commerce, National Institute of Standards and Technology, 1991.

[85] Jensen, H, Soloviev, A, Li, Z, Sogaard, E. G.; "XPS and FTIR investigation of the surface properties of different prepared titania nano-powders" *Applied Surface Science* 2005, 246, 239.

[86] Kim, B., Kim, J., Jung, B.; "Morphology and transport properties of protons and methanol through partially sulfonated block copolymers" *Journal of Membrane Science* 2005, 250, 175.

[87] Plueddemann, E. P.; "Reminiscing on silane coupling agents" *Journal of Adhesion Science and Technology* 1991, 2nd ed. New York: Plenum Press, (chapter 2).

[88] Arkles, B.; "Commercial applications of sol-gel-derived hybrid materials" *MRS Bulletin* 2001, 26(5), 402.

[89] Li, C., Wu, J., Zhao, J., Zhao, D., Fan, Q.; "Effect of inorganic phase on polymeric relaxation dynamics in PMMA/silica hybrids studied by dielectric analysis " *European Polymer Journal* 2004, 40, 1807.

[90] Kalakkunnath, S., Kalika, D. S., Lin, H. Q., Freeman, B. D.; " Viscoelastic characteristics of UV polymerized poly(ethylene glycol) diacrylate networks with varying extents of crosslinking" *Journal of Polymer Science-Part B: Polymer Physics* 2006, 44(15), 2058.

[91] Kucera, F., Jancar, J.; "Homogeneous and heterogeneous sulfonation of polymers: A review" *Polymer Engineering and Science* 1998, 38(5), 783.

[92] Chen, N. P., Hong, L.; " A study on polypyrrole-coated polystyrene sulfonic acid microspheres - a proton electrolyte " *European Polymer Journal* 2001, 37(5), 1027.

[93] Mauritz, K. A., Blackwell, R. I., Beyer, F. L.; "Viscoelastic properties and morphology of sulfonated poly(styrene-b-ethylene/butylene-b-styrene) block copolymers (sBCP), and sBCP/[silicate] nanostructured materials" *Polymer* 2004, 45(9), 3001.

[94] Yang, J. E., Lee, J. S.; "Selective modification of block copolymers as proton exchange membranes " *Electrochimica acta* 2004, 50(2-3), 617.

[95] Wu, D., Yang, Z., Wei, F., Matsumoto, M. ; "The Preparation and Magnetic Properties of Strontium Ferrite Thin Film for High Density Recording" *Physica Status Solidi (a)* 2001, 184(1), 157.

[96] Hessien, M. M., Rashad, M. M., El-Barawy, K. ; "Controlling the composition and magnetic properties of strontium hexaferrite synthesized by co-precipitation method" *Journal of Magnetism and Magnetic Materials* 2008, 320, 336.

[97] Arajs, S., Amin, N., Anderson, E. E.; "Magnetic coercivity of Fe_3O_4 particle-systems" *Journal of Applied Physics* 1991, 69, 5122.

[98] Dunlop, D. J.; "The rock magnetism of fine particles" *Physics of the Earth and Planetary Interiors.* 1981, 26, 1.

[99] Lu, A. H., Salabas, E. L., Schuth, F.; "Magnetic nanoparticles: Synthesis, protection, functionalization, and application " *Angewandte Chemie-International Edition* 2007, 46, 1222.

[100] Cornell, R. M., Schwertmann, U.; "The Iron Oxides: Structure, Properties, Reactions, Occurrence and Uses" 2003, Weinheim, Wiley-VCH, p 175.

[101] Watzky, M. A., Finke, R. G.; "Transition metal nanocluster formation kinetic and mechanistic studies. A new mechanism when hydrogen is the reductant: Slow, continuous nucleation and fast autocatalytic surface growth " *Journal of the American Chemical Society* 1997, 119, 10382.

[102] Watzky, M. A., Finke, R. G.; "Nanocluster size-control and "magic number" investigations, experimental tests of the "living-metal polymer" concept and of mechanism-based size-control predictions leading to the syntheses of iridium(0) nanoclusters centering about four sequential magic numbers " *Chemistry of Materials* 1997, 9, 3083.

[103] Overbeek, J. T. G.; "Monodisperse colloidal systems, fascinating and useful" *Advances in Colloid and Interface Science* 1982, 15, 251.

[104] Yu, W. W., Falkner, J. C., Yavuz, C. T., Colvin, V. L.; " Synthesis of monodisperse iron oxide nanocrystals by thermal decomposition of iron carboxylate salts " *Chemical Communications* 2004, 20, 2306.

[105] Roca, A. G., Morales, M. P., Serna, C. J.; "Synthesis of monodispersed magnetite particles from different organometallic precursors " *IEEE Transactions on Magnetics* 2006, 42, 3025.

[106] Goya, G. F., Berquo, T. S., Fonseca, F. C., Morales, M. P.; " Static and dynamic magnetic properties of spherical magnetite nanoparticles" *Journal of Applied Physics* 2003, 94, 3520.

[107] Jana, N. R., Chen, Y. F., Peng, X. G.; "Size- and shape-controlled magnetic (Cr, Mn, Fe, Co, Ni) oxide nanocrystals via a simple and general approach" *Chemistry of Materials* 2004, 16(20), 3931.

[108] *Powder Diffraction File Alphabetical Index* Swarthmore, Pa.: JCPDS, International Centre for Diffraction Data.

[109] Murray, C. B., Sun, S. H., Gaschler, W., Doyle, H., Betley, T. A., Kagan, CR.; "Colloidal synthesis of nanocrystals and nanocrystal superlattices" *IBM Journal of Research and Development* 2001, 45(1), 47.

[110] Kovalenko, M. V., Bodnarchuk, M. I., Lechner, R. T., Hesser, G., Schaffler, F., Heiss, W.; "Fatty acid salts as stabilizers in size- and shape-controlled nanocrystal synthesis: The case of inverse spinel iron oxide " *Journal of the American Chemical Society* 2007, 129(20), 6352.

[111] Wilhelm H. von Aulock, Arnold S. Boxer, John F. Ollom and Robert F. Rauchmiller; *Handbook of Microwave Ferrite Materials* New York, Academic Press, 1965.